A Diversity of Interneurons and Hebbian Plasticity Facilitates Rapid Compressible Learning in Hippocampus

Wilten Nicola[1] and Claudia Clopath[1*]

[1]*Imperial College London, Department of Bioengineering*
[*]*Corresponding Author: c.clopath@imperial.ac.uk*

Abstract

The hippocampus is able to rapidly learn incoming information, even if that information is only observed once. Further, this information can be replayed in a compressed format in either forward or reverse modes during Sharp Wave Ripples (SPW-Rs). We leveraged state-of-the-art techniques in training recurrent spiking networks to demonstrate how primarily interneuron networks can: 1) generate internal theta sequences to bind externally elicited spikes in the presence of inhibition from Medial Septum, 2) compress learned spike sequences in the form of a SPW-R when septal inhibition is removed, 3) generate and refine high-frequency assemblies during SPW-R mediated compression, and 4) regulate the inter-ripple-interval timing between SPW-Rs in ripple clusters. From the fast timescale of neurons to the slow timescale of behaviours, interneuron networks serve as the scaffolding for one-shot learning by replaying, reversing, refining, and regulating spike sequences.

1 Introduction

Shortly after watching a movie, we can recall many scenes in detail and remember long stretches of dialogue. However, as time passes, our memories may only preserve some aspects of the plot and a few memorable lines. This example illustrates how memories operate on separate timescales. On the short timescale, we remember recent events clearly with only a single viewing, while we lose finer details on longer timescales.

This observation, among others, led to the two-stage model of memory formation [1, 2]. In the initial stage, a labile form of the memory is imprinted onto the hippocampus. This initial acquisition is accompanied by a theta oscillation in the hippocampal Local Field Potential (LFP). The second stage of memory formation occurs during consummatory behaviours such as sleeping or eating. In this stage, strongly correlated activity is initiated in the hippocampus as a Sharp-Wave-Ripple Complex (SPW-R). The spike sequence elicited by the stimulus during waking is replayed in compressed time during SPW-Rs [3]. The SPW-R propagates out of the hippocampus, presumably for long-term memory consolidation in cortex.

This two-stage model requires some mechanism for the initial memory formation. This initial mechanism should handle the fact that we often only see a stimulus once [4]. Furthermore, this hypothesized fast-learning mechanism should allow for compressible spiking, as observed in SPW-Rs. Finally, this mechanism should allow for the reversal of spike sequences. Spike sequences can be compressed in reverse order, even for mice navigating novel mazes in the initial lap [5].

What known hippocampal dynamics allows for learning subject to these constraints? Narrowing our focus to episodic memory formation yields one possible candidate, the Internally Generated Theta Sequence (IGTS) [6, 7]. First reported in CA1, these cells partition time during episodic memory tasks [6]. The IGTSs are dependent on the Medial Septum (MS) and the hippocampal theta oscillation for normal functioning [7]. Here, we explore the hypothesis that IGTSs may serve as a compressible backbone to bind information to during single-trial-learning.

Leveraging recent advances in training spiking neural networks [8], we construct networks of phase precessing IGTSs using a dual oscillator model [9, 10]. Unlike previous dual oscillator models, we consider a novel implementation: one oscillator corresponds to inhibition from the medial septum, while another oscillator corresponds to interneuron control of spike-times during SPW-Rs. In effect, the interference between these oscillators serves to dilate spike sequences during SPW-Rs to create IGTSs. The IGTS binds new, stimulus-evoked sequences in a single-trial to form memory engrams that can be compressed and reversed in time. Our results support a single interneuron mechanism for gating, controlling, transforming and refining spike sequences for rapid learning.

2 Results

2.1 Internally Generated Theta Assemblies with Network-Based Dual Oscillators

The network model consists of three layers which we construct and analyze incrementally: the inputs, the Septal-Hippocampal-Oscillatory-Theta or SHOT network, and the readout layer. The inputs serve as one of the oscillators. The next layer, the SHOT network, is the critical nucleus of the circuit that creates IGTS and SPW sequences. The SHOT network contains the second oscillator. The final layer is the readout layer where sequences must be learned in a single-trial. These to-be-learned-sequences are elicited by an externally applied supervisor.

Thus, given the architecture of this network model, we interpret these components to correspond to the Medial Septum (INP-MS, input layer), hippocampal area CA3 (SHOT-CA3), and CA1 (RO-CA1). Finally, we interpret the supervisor which elicits spiking in the RO-CA1 layer to be the entorhinal cortex (SUP-EC, supervisor). The interference pattern or "beat" between the SHOT-CA3 network oscillator and the INP-MS oscillator creates IGTSs, while removal of INP-MS creates compressed sequences (SPWs).

This is our interpretation of an inherently abstract model which we implement in a spiking network. However, this implementation is not unique. For example, the sources of these oscillations could entirely be intra-hippocampal (see [11, 12]). Additionally, given that only inhibitory connections are required for sequence generation in the SHOT network, it may be contained in CA1.

To model the oscillatory and inhibitory nature of MS, the SHOT-CA3 interneurons (SHOT-CA3I) receive the INP-MS signal:

$$I_{MS}(t) \quad = \quad I^{GABA}\left(\kappa + \cos(2\pi\theta_{MS}t)\right). \tag{1}$$

The parameter θ_{MS} is the theta oscillation frequency of INP-MS, $\kappa \geq 1$ controls the baseline inhibition levels, and $I^{GABA} < 0$ controls the amplitude of this oscillation.

Next, the IGTSs observed in [6] generate sequential firing-fields on a behavioural timescale, while neurons oscillate at a theta frequency inside the field [6]. The spiking rate within a field is slightly faster than the LFP theta frequency, an effect termed phase precession [6, 10]. Unlike previous works [11–13], we take the perspective that firing-fields are created by septal-hippocampal interference of oscillators. This is motivated by recent work that supports intra-hippocampal theta oscillations [14–16].

Thus, we hypothesized that INP-MS could interact with a recurrent interneuron network that oscillates at a frequency of θ_{INT} (INT for Interneuron) to generate a robust interference pattern. To avoid exhaustive parameter searches, we used supervised training methods ([8]) to couple the interneurons. We successfully FORCE trained a population of spiking neurons to oscillate a frequency of θ_{INT}, while simultaneously receiving INP-MS (Figure 1A, Supplementary Figure 1, Materials and Methods, 2000 excitatory and 2000 inhibitory integrate-and-fire neurons, training only the inhibitory weights). The excitatory neurons (SHOT-CA3E) receive inputs from the interneurons (SHOT-CA3I) but do not project excitatory connections at this stage. They are driven to spike due to a constant super-threshold background current (in lieu of dentate gyrus inputs). However, their spike times are gated by SHOT-CA3I.

Post-training, when INP-MS is present, the SHOT-CA3I fire sequential bursts every theta cycle (Figure 1B,D). The SHOT-CA3E, however, display isolated firing fields on a behavioural timescale (Figure 1B,D). Population activities displayed minimal signs of the interference (Figure 1C) and are instead locked to the INP-MS frequency, θ_{MS}. This phase locking of population activities to INP-MS is a consequence of the dual oscillator model(Materials and Methods) and neurons having a uniform phase preference with regards to the θ_{INT} oscillator (Supplementary Figure 2A,B). Removal of INP-MS results in a flat population activity (Figure 1B) with a small oscillatory component at a frequency of θ_{INT} which will decrease for larger networks.

Theta-Phase and SPW-R Compression in the SHOT-CA3 Network

When INP-MS is on, the SHOT-CA3E fire IGTSs while the SHOT-CA3I fire bursts (Figure 1D). When INP-MS is off, the SHOT-CA3E also fire sequential bursts when provided with a sufficiently large (but constant) background current (Figure 1E). The burst sequence was identical to the IGTS, but compressed in time. Thus, we naturally interpret these two network states as the theta and SPW state, respectively.

Sequence compression is a consequence of the dual oscillator model. For example, when INP-MS is off, the non-dimensionalized (Materials and Methods) current is

$$z(t) \quad = \quad \cos(2\pi\theta_{INT}t + \psi) \tag{2}$$

where ψ denotes the phase preference of a neuron with respect to the θ_{INT} oscillator. The phase preference dictates a neurons firing order in the compressed SPW sequence. When INP-MS is on, the current is

$$z(t) = \cos(2\pi\theta_{MS}t) + \cos(2\pi\theta_{INT}t + \psi) \tag{3}$$

$$= \underbrace{2\cos\left(2\pi t\left(\frac{\theta_{INT} + \theta_{MS}}{2}\right) + \frac{\psi}{2}\right)}_{C(t)}\underbrace{\cos\left(2\pi t\left(\frac{\theta_{INT} - \theta_{MS}}{2}\right) + \frac{\psi}{2}\right)}_{E(t)}. \tag{4}$$

The sum becomes a product of a carrier ($C(t)$) and envelope ($E(t)$) function. Note, again, that the currents are dimensionless and lack amplitude terms (e.g. I^{GABA}). The envelope oscillates on a long timescale ($\frac{\theta_{INT} - \theta_{MS}}{2}$) and controls the IGTS firing-fields. The envelope inherits an identical order of firing from the θ_{INT} oscillator through its phase, $\frac{\psi}{2}$ when $\theta_{INT} > \theta_{MS}$. This allows for SPW-R-like compression of the IGTS by removing INP-MS (Supplementary Figure 2).

In order to determine how the SHOT-CA3I control spike sequences, we analyzed the currents that the neurons receive (Figure 1F). The total current to the SHOT-CA3E displayed characteristics of an interference pattern, as expected. However, the SHOT-CA3I did not. Their current was dominated by a single oscillation, θ_{INT}. This was surprising as the SHOT-CA3I directly receive INP-MS and generate the θ_{INT} oscillation, unlike the excitatory neurons.

We investigated this further by decomposing the total current into all sources: the background current, the SHOT-CA3I-synaptic current, and INP-MS (Figure 1G). For both populations, the inhibitory synaptic currents display an interference pattern. One oscillator is θ_{INT}. The second oscillator, however, does not correspond to INP-MS directly, but instead to a π phase-shifted or vertically "flipped" version of INP-MS. As the SHOT-CA3I also receive INP-MS directly, INP-MS destructively interferes with its phase-shifted counterpart, allowing SHOT-CA3I to oscillate at θ_{INT}.

Next, we investigated the structure of the FORCE trained weight matrices. At first, the weights appeared to be random (Supplementary Figure 3A-B). However after sorting neurons according to their phase preferences in θ_{INT}, a spatial structure emerged (Supplementary Figure 3A-B). We observed recurring light and dark bands in the weight matrix, in addition to random, phase-independent inhibitory connections. The random connections sample from the entire SHOT-CA3I. By receiving these connections, a neuron can detect the population level oscillation in θ_{MS} for destructive interference (Materials and Methods). The banding structure, however, implies interneurons preferentially inhibit interneurons that already fired in θ_{INT}, thus advancing the θ_{INT} oscillation forward. This band reappeared in multiple trials of FORCE training (Supplementary Figure 3C-F).

Finally, by using either the INP-MS oscillation (not shown) or the population activity (Figure 1H,I) as a reference theta oscillation, both excitatory neurons and interneurons precess in phase. This is a classical result of dual oscillator models as the carrier, $C(t)$, controls the spike timing in the IGTS [10]. As the carrier oscillates faster than INP-MS ($\frac{\theta_{INT} + \theta_{MS}}{2} > \theta_{MS}$), the neurons precess in phase relative to the population activity (average rate precession $\approx -\frac{\pi}{2}/s$, SD of $0.09\pi/s$ $n = 100$, SHOT-CA3E, and $\approx -0.91\pi/s$, SD of $0.4\pi/s$, $n = 100$, SHOT-CA3I).

2.2 Firing Field Generation is Robust

For the IGTSs to serve as a compressible backbone for learning, the interference mechanism should be robust. To that end, we retrained the network under different conditions such as with 1) smaller integration time steps (Supplementary Figure 4), 2) parameter heterogeneity (Supplementary Figure 5) 3) larger networks (Supplementary Figure 6C), and 4) different SHOT-CA3E/SHOT-CA3I ratios (Supplementary Figure 6A-B,D-E) and 5) synaptic failure (Supplementary Figure 7). In all cases, the network generated ordered IGTSs that compressed when INP-MS was removed and a weight matrix banding structure (Supplementary Figure 5,6).

Next, we considered how the trained network (in Figure 1) would extrapolate to varied θ_{MS} frequencies. If SHOT-CA3 was operating as a linear oscillator, we should expect that the firing-field periodicity scales like $|\theta_{MS} - \theta_{INT}|^{-1}$ near θ_{INT}, while the population activity has a period of θ_{MS}^{-1}. Furthermore, our model predicts that IGTS order reverses when $\theta_{MS} > \theta_{INT}$ (Materials and Methods). This regime should also induce phase recession. Finally, we also predict firing fields to emerge near harmonics of θ_{INT}. To test this hypothesis, we slowly swept θ_{MS} (2 Hz to 12 Hz, Supplementary Figure 8). We found that SHOT-CA3 behaves like a linear oscillator for θ_{MS} tested. This surprising ability to extrapolate to new inputs is due to the SHOT-CA3I ability to create destructive interference of any input to maintain the θ_{INT} oscillator. The firing fields also reverse near the harmonics of θ_{INT}. Thus, θ_{MS} directly determines the frequency of the population activity, as predicted from a dual oscillator model.

Finally, ramping the background current to the interneurons has no effect on the frequency of the population activity and a small yet statistically significant effect on the period of the interference pattern (Supplementary Figure 9). However, a stronger reduction in the background current destroys θ_{INT} and causes SHOT-CA3I to lock onto INP-MS (not shown). This mirrors recent results where optogenetic suppression of interneurons reduces phase precession rates but increases intracellular theta amplitude [17]. Ramping the INP-MS oscillation amplitude (I^{GABA}) has a large and statistically significant effect on the periodicity of the IGTSs and a small yet significant effect on the frequency of the population activity (Supplementary Figure 9). Thus, the network is sensitive to large modulations of the INP-MS amplitude but robust to θ_{MS} variations.

2.3 Sharp Waves Can Be Initiated Stochastically

So far, the SPWs induced in our model (when INP-MS is deactivated) are periodic and must be activated by an externally applied current as INP-MS dis-inhibits the SHOT-CA3E. We investigated if SPWs could be initiated stochastically when INP-MS is off by adding recurrent excitation to the SHOT-CA3E. Once again, we will do this incrementally to mechanistically understand how ordered SPWs are generated in the SHOT-CA3 network.

First, in lieu of constant background current, we injected SHOT-CA3I with white noise (Figure 2A-D). All inhibitory connections are identical as before (as in Figure 1). A current pulse to SHOT-CA3I can transiently activate the θ_{INT} oscillator. In the absence of this current, the θ_{INT} oscillator is destroyed by the noise as the oscillator is no longer detected in FORCE oscillator components (Figure 2B), voltage traces (Figure 2C), and voltage auto-correlations (Figure 2D). However, the spikes are still biased towards a particular order as noise percolates through the inhibitory weight structure for both populations (Figure 2B).

Next, we investigated potential mechanisms that could initiate and terminate a SPW in lieu of externally applied currents (in Figure 2B). To initiate a SPW, we densely coupled a subset of 50 SHOT-CA3E (the initiators). The initiators projected to the rest of the excitatory population. To terminate SPWs, all excitatory neurons had spike frequency adaptation currents. As noise induces spiking throughout the network, a random subset of initiators are stimulated to spike (Figure 2E-G). This triggers a positive feedback loop through recurrent excitation which causes a synchronized burst throughout SHOT-CA3E. However, this triggers the accumulation of adaptation currents which terminate the burst. This induces a refractory period where SHOT-CA3E cannot spike until the adaptation current has decayed. As the θ_{INT} oscillator has not been activated, the spikes in the bursts have no sequential ordering and are pathologically synchronized.

Finally, we add SHOT-CA3E to SHOT-CA3I connections (Figure 2H). The SHOT-CA3E self-activate through recurrent excitation and now also activate the θ_{INT} oscillator (Figure 2I-J). The θ_{INT} oscillator protracts the recruitment SHOT-CA3E into the burst, thereby creating an ordered sequence during the SPW rather than synchronized bursts. The adaptation variable then terminates the burst. The resulting inter-SPW-interval distributions can be uni-modal with varying amounts of skew, or multi-modal (Supplementary Figure 10). Thus, SPWs can be activated stochastically with interneurons protracting the recruitment of excitatory neurons into the ordered burst.

2.4 Reverse Compressed Replay

Given that the IGTS is compressible, we investigated if reverse compression was also possible, as in other models [3, 18]. We discovered three potential mechanisms for reverse compression (Figure 3). The first two mechanisms (harmonic reversion, and mirror reversion) are based on manipulations to the INP-MS frequency to reverse the order during the IGTS. The third mechanism utilizes a secondary population of interneurons (interneuron reversion) to reverse the order of spiking in SHOT-CA3E during the SPW.

In mirror reversion, the frequencies satisfy $\theta_{MS} > \theta_{INT}$ which reverses IGTS order (Figure 3A-E) as $E(t)$ now inherits $-\frac{\psi}{2}$ from the θ_{INT} oscillation. Removing of INP-MS reverses burst order during compressed replay (Figure 3C). However, this is not a plausible mechanism as this results in phase recession and reversed theta sequences (Figure 3D), seldom observed experimentally[19, 20]. Harmonic reversion is possible when θ_{MS} is near harmonics of θ_{INT}, where IGTS order also reverses. For harmonics smaller than θ_{INT}, this does not induce phase recession. However, memories encoded onto the IGTS under mirror/harmonic Reversion only display reverse replays as the SPW sequence order is fixed, while both forward and reverse sequences are observed in SPWs [3, 5].

However, a more plausible mechanism for reverse compression utilizes another population of interneurons. During SPWs, excitatory neurons receive the non-dimensionalized currents $z^{FOR}(t)$ from the θ_{INT} oscillator:

$$z^{FOR}(t) = \cos(2\pi\theta_{INT} + \psi). \tag{5}$$

4

The phase preference, ψ, orders the neurons in a sequence. Thus, a reverse replay is equivalent to replacing ψ with $-\psi$.

To perform this transform, we utilize another interneuron current (the Reversion Current) where the total current during reverse replay is now:

$$z^{REV}(t) = \cos(2\pi\theta_{INT} - \psi) = z^{FOR}(t) + \underbrace{2\sin(\psi)\sin(2\pi\theta_{INT}t)}_{\text{Reversion Current}} \tag{6}$$

The reversion current we add to Equation (5) is a synchronized pulse of the θ_{INT} oscillator. However, each neuron receives more or less of this pulse through the amplitude term $2\sin(\psi)$. Thus, we implement the reversion current as another population of interneurons that receives SHOT-CA3I (Figure 3F-J). This reverses the excitatory SHOT-CA3 sequences when INP-MS is removed (Figure 3H-I, see Materials and Methods). The pulse amplitude $2\sin(\psi)$ need not be exact for (Supplementary Figure 11). The reversion interneurons may also receive INP-MS to prevent their firing during theta states (see Supplementary Figure 11). Further, phase recession is not observed in Interneuron Reversion (Figure 3J). Thus, interneurons with selective connectivity can reverse the timing of spike-timing during SPWs in a plausible way.

2.5 Online and Immediate Learning Using a Theta Backbone

Compressible theta sequences are one component of fast learning in this model. The other component is a mechanism to write new information onto these sequences. Reading out information falls to a layer of readout (RO-CA1) neurons, which we interpret to be CA1 pyramidal neurons (Figure 4A).

We derived a local learning rule that allows us to store new sequences in RO-CA1 onto the IGTSs in SHOT-CA3 with only one presentation of the to-be-learned RO-CA1 sequences. The learning rule governing the excitatory weight ($\omega_{pre,post}^{CA1E,CA3E}$) from a SHOT-CA3E to a RO-CA1 neuron is given by:

$$\dot{\omega}_{pre,post}^{CA1E,CA3E} = \lambda \cdot \boldsymbol{r}_{pre}^{CA3E}(t)\boldsymbol{r}_{post}^{CA1E}(t) - \lambda \cdot \boldsymbol{r}_{pre}^{CA3E}(t)\boldsymbol{r}_{post}^{CA1E}(t - \tau) \tag{7}$$

This learning rule is Hebbian ($\lambda \cdot \boldsymbol{r}_{pre}^{CA3E}(t)\boldsymbol{r}_{post}^{CA1E}(t)$), with a forgetting term ($\lambda \cdot \boldsymbol{r}_{pre}^{CA3E}(t)\boldsymbol{r}_{post}^{CA1E}(t - \tau)$), where λ dictates the learning rate and $r_{pre/post}^{CA3E/CA1E}(t)$ are the synaptically filtered spikes. The learned weights are interpreted to be Schaffer-Collateral connections. We call this the local Fourier rule based on its origins in function approximation theory (see Supplementary Figure 12, Supplementary Section S1). Like other rules, this rule is phenomenological [21, 22].

To test the local Fourier rule, we triggered to-be-learned sequences in RO-CA1 while simultaneously presenting INP-MS (Figure 4B,C) to SHOT-CA3, (Equation (7)). We interpret the external activity which causes the to-be-learned sequences to come from the Entorhinal Cortex (SUP-EC, SUP for supervisor). Critically, the $\omega_{pre,post}^{CA3E,CA3I}$ weights are too weak to trigger spikes in the presence of INP-MS and do not interfere with SUP-EC triggered spikes. However, if INP-MS is removed, RO-CA1 sequences are replayed in compressed sequential order after a single-trial of learning (Figure 4D).

Surprisingly, this compression does not capture all spikes in RO-CA1. In fact, the local Fourier rule combined with IGTSs creates high-frequency assemblies in RO-CA1 during compressed replay (Figure 4D,F). This is due to the Hebbian learning rule as only RO-CA1 neurons that fired in phase with SHOT-CA3E are remembered. The frequency of assembly firing is $\Gamma = \theta_{MS} + \frac{\theta_{MS}^2}{\theta_{INT}-\theta_{MS}}$ (Materials and Methods). For the parameters we have chosen, this yields $\Gamma = 136$ Hz. Lower frequency ranges, including within the gamma range, are possible with smaller values of θ_{MS} for a fixed θ_{INT}.

Our result implies that theta oscillations and Hebbian plasticity can induce the formation of high-frequency assemblies, which appear during SPWs. Unlike other mechanisms of high-frequency oscillations [23–25], the assemblies here are learned through Hebbian plasticity operating on phase precessing IGTSs rather than recurrence, or different populations serving as separate gamma and theta oscillators [26]. Stimulating the reversion interneurons triggers a reverse replay of these assemblies (Figure 4E). More complicated spiking patterns can also be learned (Figure 4G).

Finally, we show that the local Fourier rule is robust to synchronized supervisors (Supplementary Figure 13), non-uniform phase distributions in SHOT-CA3 (Supplementary Figure 5A-C), heterogeneity in SHOT-CA3 (Supplementary Figure 5D-F), different E/I balances in SHOT-CA3 (Supplementary Figure 6), and synaptic failure in SHOT-CA3 (Supplementary Figure 7). Our model implies that MS inhibition in conjunction with Hebbian plasticity can regulate spike timing on the short (gamma and higher), intermediate (theta), and long (behavioural) timescales simultaneously.

2.6 Triggering Sharp-Wave Ripples

With the network layers constructed and analyzed, we add the final component to the model: interneurons in RO-CA1. The RO-CA1 excitatory neurons (RO-CA1E) excite RO-CA1 interneurons (RO-CA1I) while RO-CA1I inhibits RO-CA1E (Figure 5A) [23, 24].

The RO-CA1E were (as in Figure 4) stimulated to spike in a to-be-learned sequence by SUP-EC (Figure 5C). The local Fourier rule constructed a memory engram in a single trial. The INP-MS was removed and triggered a compressed replay of the now-learned sequence (Figure 5B-D). The population activity (Figure 5F) in RO-CA1 displayed ripple-like high-frequency oscillations during compression. The activity in SHOT-CA3, however, demonstrated a sharp increase when INP-MS was removed (Figure 5G). This is a combined effect of removing INP-MS from SHOT-CA3I and applying a super-threshold current to SHOT-CA3E. Compression resulted in high-frequency assembly formation in RO-CA1E (Figure 5C,D) while RO-CA1I fired high-frequency synchronous volleys (Figure 5E). The number of RO-CA1E assemblies was less than the number of bursts triggered in RO-CA1I (8 vs. 10).

The majority of the activity is due to RO-CA1I which are locked to the population activity ripples (Figure 5H). If we regard the population activity as a proxy (albeit a poor one) for the LFP, then our results mirror PV-basket cells locking to LFP ripples [27, 28]. The RO-CA1E assemblies also display some locking to the ripples (Figure 5H). However, the assemblies precede the ripple peaks as RO-CA1E synapses onto RO-CA1I trigger the synchronized ripples. This is similar to the Pyramidal Interneuron Network Gamma (PING) mechanism [23, 24].

As SHOT-CA3 and Reversion interneurons coordinated spike timing, we investigated if RO-CA1I performed a similar function. To test this hypothesis, we disabled RO-CA1I post-learning while triggering a compressed replay (Figure 5I) by removing INP-MS. The assemblies in RO-CA1E were no longer segregated to discrete moments in time and overlapped extensively. In fact, the first assembly overlapped with the last assembly during replay. This implies that RO-CA1I may be refining the duration of learned pyramidal assemblies and segregating them to discrete intervals of time (Figure 5J) with strong, synchronized pulses of inhibition. Indeed, in vivo, it appears that pulses of inhibition dominate during ripples in CA1 over excitation [29]. This may help to transmit information reliably out of the hippocampus. It is possible to manually separate these assemblies, for example (as in Figure 4D). However, adding interneurons in RO-CA1 in these cases will still refine assembly segregation further (as in Figure 5D,I). As with SHOT-CA3 and Reversion interneurons, our results support the idea that interneurons in CA1 also regulate spike-timing by refining the width of learned assemblies in CA1 via a PING-like mechanism [23, 24].

2.7 High-Frequency Assemblies Nested on a Theta Oscillation

Assembly discretization occurs during SPW-Rs in our model. However, gamma oscillations (of varying frequency) are often nested with theta and implicated in memory tasks [30, 31]. These gamma oscillations are also found during SPW-Rs [3, 32, 33]. Thus, we investigated if high-frequency assemblies would persist in theta states (Supplementary Figure 14).

Providing a stronger background current to SHOT-CA3E results in RO-CA1E firing as phase precessing assemblies nested on theta. This occurs after learning with the local Fourier rule (as in Figure 5). Thus, theta phase segregation and Hebbian learning rules can generate theta-nested assemblies. This is similar to the operations of a working memory buffer (suggested in [34]). Here, the number of assemblies/items in this buffer is

$$N_{items} \leq \frac{\theta_{MS}}{\theta_{INT} - \theta_{MS}}. \tag{8}$$

The period of the INP-MS oscillation $(\theta_{MS})^{-1}$ acts as the buffer's temporal resolution while the IGTS period $(\theta_{INT} - \theta_{MS})^{-1}$ determines the capacity of the buffer (Materials and Methods). Our model parameters yield a maximum of 16 items in the buffer.

2.8 Ripple-Clusters Minimize Fragmentation of Memories

Finally, we investigated how stochastic SPW-R initiation would alter replays [3, 35].

Here, we consider a more controlled and phenomenological model of stochastic SPW-R activation, rather than recurrent excitation (considered in Figure 2). We disabled INP-MS post-learning and stochastically turned on extra excitation to initiate SPW-Rs (Figure 5K). This phenomenological model of SPW-Rs initiation caused random replays of the learned memory (seen in Figure 5K). We found that depending on when the SPW-R was

initiated, replays could display an error we term phase distortion. In phase distortion, the replay is fragmented into disordered pieces. Phase distortion occurs when SPW-Rs are initiated in the wrong phase of θ_{INT} (Figure 5K). To reduce phase distortions, SHOT-CA3I can bias the probability of SPW initiation to the correct phase range of θ_{INT}. We considered the probability $p(t)$ of initiating a SPW-R as

$$p(t) = p_0 + p_A \cos(2\pi\theta_{INT}t + \psi_i) \tag{9}$$

where ψ_i is the phase that minimizes phase distortion. The parameter p_0 serves as the background SPW activation rate and p_A determines how strong the SPW generation probability oscillates. The oscillatory component is decoded from SHOT-CA3I (see Materials and Methods). A relative refractory period was also incorporated (see Materials and Methods). This strategy to minimize phase distortions has an observable effect on inter-SPW-R-interval distributions. The inter-SPW-R-intervals now display a strong θ_{INT} modulation (Figure 5L). This is qualitatively similar to distributions recently reported in [36] which are multi-modal with peaks at 110 ms, 220 ms, 330 ms, and 440 ms. The inter-SPW-R-intervals from [36] may imply some theta modulation in SPW-R initiation with a potential $\theta_{INT} \approx 9.1$ Hz. Thus, our results support the idea that inhibition can also influence SPW-R initiation and inter-SPW-R-interval distributions to minimize replay fragmentation.

3   Discussion

Our memory systems have to handle multiple simultaneous constraints to record, store, and catalog important events. One constraint is that stimuli are often presented only once. Thus, we investigated whether single-trial learning was possible utilizing background spiking activity as a backbone for learning. The background spiking activity took the form of the Internally Generated Theta Sequence (IGTS) [6, 7], generated with a dual oscillator model. We interpreted one oscillator as intra-hippocampal that controlled spike timing during SPWs. The second oscillator was externally applied and interpreted as the Medial Septum (MS). We found that this was sufficient to create stable firing-fields in pyramidal, but not interneurons. Removal of the INP-MS oscillator can trigger compression of the firing-fields as ordered bursts. A dedicated population of interneurons can also induce reverse replays.

We derived a local learning rule that could successfully bind to-be-learned sequences that were generated by external inputs onto the IGTS. Forward or reverse replays could be induced by removing the INP-MS. Surprisingly, through a combination of the local Fourier rule and theta oscillations during learning, high-frequency assemblies emerged during replays. These assemblies also persisted in the presence of MS inhibition, where they nested on the theta oscillation. These assemblies triggered ripple-like oscillations in RO-CA1. The RO-CA1I were the dominant component of the population activity and displayed phase locking to the ripples in the population activity. The ripples served to segregate learned assemblies and prevent assembly overlap. Finally, we demonstrated that SHOT-CA3I can prevent memory fragmentation due to phase distortions during replay by modulating the probability of SPW-R initiation. We predicted that this would have an observable effect on inter-SPW-R interval distributions that has been observed experimentally [36]. Our results support the role of interneurons in generating, compressing, reversing, and refining spike sequences for stable learning.

A Link Between Theta-Phase Compression and Sharp-Wave-Ripple Compression

Our results suggest that the mechanism for SPW-R compression and compression within a theta cycle may be one and the same. The timing of spikes during both events can be coordinated by a single population of interneurons, operating in two modes, which are delineated by the presence of MS inhibition. When INP-MS was present, the sequence compression within a theta cycle is due to the SPW regulating current, θ_{INT}.

The hypothesis that these compression mechanisms are related is supported by two lines of experimental evidence. First, the SPW-R compression ratio is only slightly larger (30%) than theta-phase compression [3, 37]. Second, in extended replay, SPW-Rs often occur in clusters containing multiple SPW-Rs [36, 38]. The individual SPW-Rs within a cluster have a 100-150 ms gap, or a theta period, between them [3, 36, 38]. Strikingly, in [36], the authors find theta-harmonics in the inter-SPW-R-interval as peaks in the distribution at 110, 220, 330, and 440 ms. It is important to note that SPW-R clusters also form due to phase locking in 7-10 Hz sleep-spindles [39]. However, SPW-R clusters are reliably evoked during quite awake, when an animal is exploring longer mazes [36, 38].

Experimental Predictions from Our Model

We suggest a novel experiment to assess whether dual oscillators support IGTSs. First, employing the left/right alternation task as in [6] should yield stable firing-fields during wheel running [6, 7] (Figure 6A). We suggest using a closed loop feedback system to [40–42] optogenetically drive the MS to oscillate at different frequencies during wheel running (Figure 6A). For a sufficiently large driving frequency, $\theta_D > \theta_{INT}$, interference theory predicts sequence reversal in the IGTS and phase recession (Figure 6A). For further model predictions, see supplementary discussion (Supplementary Note S1) and Table 2.

Limitations of the Model

While our model displays many of the intrinsic rhythms and behaviours of the hippocampus, like all models, it is a simplification. Here, we consider discrepancies between our model and experimental data. We list the following four limitations: 1) interneurons display limited or no phase precession, 2) the presence of attractor network dynamics in CA3, 3) the gamma/high-frequency oscillation that we predict due to CA3 is faster than observed and 4) the aperiodicity of observed IGTSs. We discuss the limitations of our model more in the supplementary discussion (Supplementary Note S1).

While pyramidal cells precess in phase under a variety of conditions [6, 10], interneuron phase precession is less clear. Some interneurons in CA1 display phase precession due to strong, monosynaptic connectivity with a phase precessing pyramidal neuron [43]. Other measurements of interneuron phase precession demonstrate a greater variability in phase precession slopes [19], with some interneurons even displaying bouts of phase recession (see Figure 3,4 in [19]). Interestingly, the authors ([19]) note that interneurons fire wider bursts which might make phase precession more difficult to assess. However, as the leaky-integrate-and-fire model has limitations in producing the rich dynamics of real neurons, interneuron phase precession in our network model may be eliminated by considering other neuron models.

Our model uses no recurrent excitatory connectivity to create sequences. The recurrent activity is used only to activate interneuron networks. Both phase precessing and SPW spike sequences are internally created in our model by inhibitory weights. While interneuron spike sequences have been documented [44], both experimental work [45] and theoretical modelling [11, 12, 46] have demonstrated that excitatory connectivity is an important factor for sequence generation and compression. It would be interesting to combine our model with attractor-like dynamics in the future.

Other Models of Replay and Theta Sequences

Dual oscillator models have been suggested as a mechanism for phase precession long before this study [10]. Other studies have considered somato-dendritic interference as a source of phase precession [47]. Recent studies have demonstrated how multiple intra-hippocampal oscillators with uniform phase clustering at discrete values could yield a slower oscillation in the global population activity [11, 12]. This mirrors our result with the continuous uniform distribution endowing INP-MS control over population activities. Here, we consider the novel hypothesis that phase precession arises from the need to dilate pre-existing SPW sequences for single-trial-learning of new sequences.

Multiple-oscillator models were also considered as a mechanism of grid cell firing [9]. In these models, the theta frequency is linked to animal velocity in velocity controlled oscillator's (VCO's). By using three VCO's with phase-shifts separated by $\frac{2\pi}{3}$, hexagonal grid patterns emerge in space. However, recent experiments have cast doubt on this mechanism as grid cells still occur in bats without theta oscillations [48]. Further, in vivo patch recordings demonstrate that an underlying ramp of depolarization encodes significantly more spatial information than the theta oscillation envelope [49, 50]. Here, we considered a different hypothesis: the interference arises between an oscillator controlling the spike-times during SPWs, and the medial septum. This creates a compressible IGTS for single-trial learning.

Finally, other models have either linked theta sequences to SPW-Rs [46] or considered the problem of fast-learning in the hippocampus. We summarize these in the supplementary discussion (Supplementary Note S1).

Conclusion

A long-standing hypothesis is that interneurons control spike timing. Here, we demonstrate how populations of interneurons can 1) generate theta oscillations in the hippocampus through recurrent and septal inhibition 2) create phase precessing theta sequences, 3) trigger compressed replay of these sequences in forward or

reversed modes 4) facilitate single-trial learning of spike trains as high-frequency-assemblies and 6) refine said assemblies by minimizing their overlap in time, 7) nest these assemblies on a theta oscillation after learning and finally 8) modulate the inter-SPW-R-intervals to prevent the replay fragmentation. This intricate control over spiking in our model was facilitated with little more than a pair of oscillators, interneuron/pyramidal reciprocal connectivity, and Hebbian plasticity.

Acknowledgments

Author Contributions

WN and CC conceived the study and wrote the manuscript. WN conducted simulations and data analysis.

Competing Interests

The authors declare no competing interests.

Bibliography

[1] Buzsáki, G. Two-stage model of memory trace formation: a role for "noisy" brain states. *Neuroscience* **31**, 551–570 (1989).

[2] McClelland, J. L., McNaughton, B. L. & O'reilly, R. C. Why there are complementary learning systems in the hippocampus and neocortex: insights from the successes and failures of connectionist models of learning and memory. *Psych. Rev.* **102**, 419 (1995).

[3] Buzsáki, G. Hippocampal sharp wave-ripple: A cognitive biomarker for episodic memory and planning. *Hippocampus* **25**, 1073–1188 (2015).

[4] Standing, L., Conezio, J. & Haber, R. N. Perception and memory for pictures: Single-trial learning of 2500 visual stimuli. *Psychonomic Science* **19**, 73–74 (1970).

[5] Foster, D. J. & Wilson, M. A. Reverse replay of behavioural sequences in hippocampal place cells during the awake state. *Nature* **440**, 680 (2006).

[6] Pastalkova, E., Itskov, V., Amarasingham, A. & Buzsáki, G. Internally generated cell assembly sequences in the rat hippocampus. *Science* **321**, 1322–1327 (2008).

[7] Wang, Y., Romani, S., Lustig, B., Leonardo, A. & Pastalkova, E. Theta sequences are essential for internally generated hippocampal firing fields. *Nat. Neuro.* **18**, 282–288 (2015).

[8] Nicola, W. & Clopath, C. Supervised learning in spiking neural networks with force trainnig. *Nat. Comms.* **8** (2017).

[9] Burgess, N., Barry, C. & O'keefe, J. An oscillatory interference model of grid cell firing. *Hippocampus* **17**, 801–812 (2007).

[10] O'Keefe, J. & Recce, M. L. Phase relationship between hippocampal place units and the eeg theta rhythm. *Hippocampus* **3**, 317–330 (1993).

[11] Geisler, C., Robbe, D., Zugaro, M., Sirota, A. & Buzsáki, G. Hippocampal place cell assemblies are speed-controlled oscillators. *Proc. of Nat. Acad. of Sci.* **104**, 8149–8154 (2007).

[12] Geisler, C. *et al.* Temporal delays among place cells determine the frequency of population theta oscillations in the hippocampus. *Proc. of Nat. Acad. of Sci.* 200912478 (2010).

[13] Hasselmo, M. E. & Stern, C. E. Theta rhythm and the encoding and retrieval of space and time. *Neuroimage* **85**, 656–666 (2014).

[14] Buzsáki, G. Theta oscillations in the hippocampus. *Neuron* **33**, 325–340 (2002).

[15] Buzsáki, G., Czopf, J., Kondakor, I. & Kellenyi, L. Laminar distribution of hippocampal rhythmic slow activity (rsa) in the behaving rat: current-source density analysis, effects of urethane and atropine. *Brain research* **365**, 125–137 (1986).

[16] Goutagny, R., Jackson, J. & Williams, S. Self-generated theta oscillations in the hippocampus. *Nat. Neuro.* **12**, 1491–1493 (2009).

[17] Grienberger, C., Milstein, A. D., Bittner, K. C., Romani, S. & Magee, J. C. Inhibitory suppression of heterogeneously tuned excitation enhances spatial coding in ca1 place cells. *Nat. Neuro.* **20**, 417 (2017).

[18] Roach, J. P. *et al.* Resonance with subthreshold oscillatory drive organizes activity and optimizes learning in neural networks. *Proc. of Nat. Acad. of Sci.* 201716933 (2018).

[19] Ego-Stengel, V. & Wilson, M. A. Spatial selectivity and theta phase precession in ca1 interneurons. *Hippocampus* **17**, 161–174 (2007).

[20] Cei, A., Girardeau, G., Drieu, C., El Kanbi, K. & Zugaro, M. Reversed theta sequences of hippocampal cell assemblies during backward travel. *Nat. Neuro.* **17**, 719 (2014).

[21] Gerstner, W., Kempter, R., van Hemmen, J. L. & Wagner, H. A neuronal learning rule for sub-millisecond temporal coding. *Nature* **383**, 76 (1996).

[22] Pfister, J.-P. & Gerstner, W. Triplets of spikes in a model of spike timing-dependent plasticity. *J. Neuro.* **26**, 9673–9682 (2006).

[23] Whittington, M. A., Traub, R., Kopell, N., Ermentrout, B. & Buhl, E. Inhibition-based rhythms: experimental and mathematical observations on network dynamics. *Int. J. of Psychophys.* **38**, 315–336 (2000).

[24] Börgers, C. & Kopell, N. Synchronization in networks of excitatory and inhibitory neurons with sparse, random connectivity. *Neural computation* **15**, 509–538 (2003).

[25] Bartos, M., Vida, I. & Jonas, P. Synaptic mechanisms of synchronized gamma oscillations in inhibitory interneuron networks. *Nat. Rev. Neuro.* **8**, 45 (2007).

[26] Pike, F. G. *et al.* Distinct frequency preferences of different types of rat hippocampal neurones in response to oscillatory input currents. *J. Phsyiol.* **529**, 205–213 (2000).

[27] Ylinen, A. *et al.* Sharp wave-associated high-frequency oscillation (200 hz) in the intact hippocampus: network and intracellular mechanisms. *J. Neuro.* **15**, 30–46 (1995).

[28] Klausberger, T. & Somogyi, P. Neuronal diversity and temporal dynamics: the unity of hippocampal circuit operations. *Science* **321**, 53–57 (2008).

[29] Gan, J., Weng, S.-m., Pernía-Andrade, A. J., Csicsvari, J. & Jonas, P. Phase-locked inhibition, but not excitation, underlies hippocampal ripple oscillations in awake mice in vivo. *Neuron* **93**, 308–314 (2017).

[30] Belluscio, M. A., Mizuseki, K., Schmidt, R., Kempter, R. & Buzsáki, G. Cross-frequency phase–phase coupling between theta and gamma oscillations in the hippocampus. *Journal of Neuroscience* **32**, 423–435 (2012).

[31] Lisman, J. The theta/gamma discrete phase code occuring during the hippocampal phase precession may be a more general brain coding scheme. *Hippocampus* **15**, 913–922 (2005).

[32] Tukker, J. J., Fuentealba, P., Hartwich, K., Somogyi, P. & Klausberger, T. Cell type-specific tuning of hippocampal interneuron firing during gamma oscillations in vivo. *J. Neuro.* **27**, 8184–8189 (2007).

[33] Csicsvari, J., Jamieson, B., Wise, K. D. & Buzsaki, G. Mechanisms of gamma oscillations in the hippocampus of the behaving rat. *Neuron* **37**, 311–322 (2003).

[34] Lisman, J. E. & Idiart, M. A. Storage of 7+/-2 short-term memories in oscillatory subcycles. *Science* **267**, 1512–1515 (1995).

[35] Schlingloff, D., Káli, S., Freund, T. F., Hájos, N. & Gulyás, A. I. Mechanisms of sharp wave initiation and ripple generation. *J. Neuro.* **34**, 11385–11398 (2014).

[36] Yamamoto, J. & Tonegawa, S. Direct medial entorhinal cortex input to hippocampal ca1 is crucial for extended quiet awake replay. *Neuron* **96**, 217–227 (2017).

[37] Diba, K. & Buzsáki, G. Forward and reverse hippocampal place-cell sequences during ripples. *Nat. Neuro.* **10**, 1241 (2007).

[38] Davidson, T. J., Kloosterman, F. & Wilson, M. A. Hippocampal replay of extended experience. *Neuron* **63**, 497–507 (2009).

[39] Sirota, A., Csicsvari, J., Buhl, D. & Buzsáki, G. Communication between neocortex and hippocampus during sleep in rodents. *Proc. of Nat. Acad. of Sci.* **100**, 2065–2069 (2003).

[40] Boyce, R., Glasgow, S. D., Williams, S. & Adamantidis, A. Causal evidence for the role of rem sleep theta rhythm in contextual memory consolidation. *Science* **352**, 812–816 (2016).

[41] Bender, F. *et al.* Theta oscillations regulate the speed of locomotion via a hippocampus to lateral septum pathway. *Nat. Comms.* **6**, 8521 (2015).

[42] Zutshi, I. *et al.* Hippocampal neural circuits respond to optogenetic pacing of theta frequencies by generating accelerated oscillation frequencies. *Curr. Biol.* (2018).

[43] Maurer, A. P., Cowen, S. L., Burke, S. N., Barnes, C. A. & McNaughton, B. L. Phase precession in hippocampal interneurons showing strong functional coupling to individual pyramidal cells. *J. of Neuro.* **26**, 13485–13492 (2006).

[44] Stark, E., Roux, L., Eichler, R. & Buzsáki, G. Local generation of multineuronal spike sequences in the hippocampal ca1 region. *Proc. of Nat. Acad. of Sci.* **112**, 10521–10526 (2015).

[45] Dragoi, G., Carpi, D., Recce, M., Csicsvari, J. & Buzsáki, G. Interactions between hippocampus and medial septum during sharp waves and theta oscillation in the behaving rat. *J. Neuro.* **19**, 6191–6199 (1999).

[46] Chenkov, N., Sprekeler, H. & Kempter, R. Memory replay in balanced recurrent networks. *PLoS Comp. Bio.* **13**, e1005359 (2017).

[47] Lengyel, M., Szatmáry, Z. & Érdi, P. Dynamically detuned oscillations account for the coupled rate and temporal code of place cell firing. *Hippocampus* **13**, 700–714 (2003).

[48] Yartsev, M. M., Witter, M. P. & Ulanovsky, N. Grid cells without theta oscillations in the entorhinal cortex of bats. *Nature* **479**, 103 (2011).

[49] Harvey, C. D., Collman, F., Dombeck, D. A. & Tank, D. W. Intracellular dynamics of hippocampal place cells during virtual navigation. *Nature* **461**, 941 (2009).

[50] Domnisoru, C., Kinkhabwala, A. A. & Tank, D. W. Membrane potential dynamics of grid cells. *Nature* **495**, 199 (2013).

A

INP-MS On: Theta Sequences

SHOT-CA3 Network

θ_{MS}

θ_{INT}

INP-MS Off: Ordered Burst Firing

SHOT-CA3 Network

θ_{MS}

θ_{INT}

△ Excitatory Neuron
○ Inhibitory Neuron
■ Inhibitory Connection
— INP-MS

B Voltage Traces

INP-MS On   Off

1 s   Excitatory   Inhibitory

C Population Activities

1 s   Excitatory   Inhibitory
Average   Total

D IGTS Firing Fields

Filtered Spike Trains

Excitatory   2000   0

Inhibitory   2000   0

1 s

E Ordered Bursts

5 Hz   0

5 Hz   0

100 ms

F Membrane Potential with Current Overlay

Voltage Traces

INP-MS On   Off   35 mv/0 pA   -70 mv/-100 pA

INP-MS On   Off   35 mv/0 pA   -70 mv/-100 pA

G Decomposition of Neuronal Currents

Currents   25 pA   -70 pA

0.5 s

25 pA   -70 pA

0.5 s

Excitatory SHOT-CA3 Neuron Voltage   Total Current to Neuron   INP-MS
Inhibitory SHOT-CA3 Neuron Voltage   Background Current to Neuron   Current from SHOT-CA3 Interneurons

H Phase Precession

Population Activity   40 Hz

1 s   Population Activity   Excitatory Neuron Spike Time   Inhibitory Neuron Spike Time

I

SHOT-CA3I Spike   SHOT-CA3E Spike

Spike Phase 2π π 0
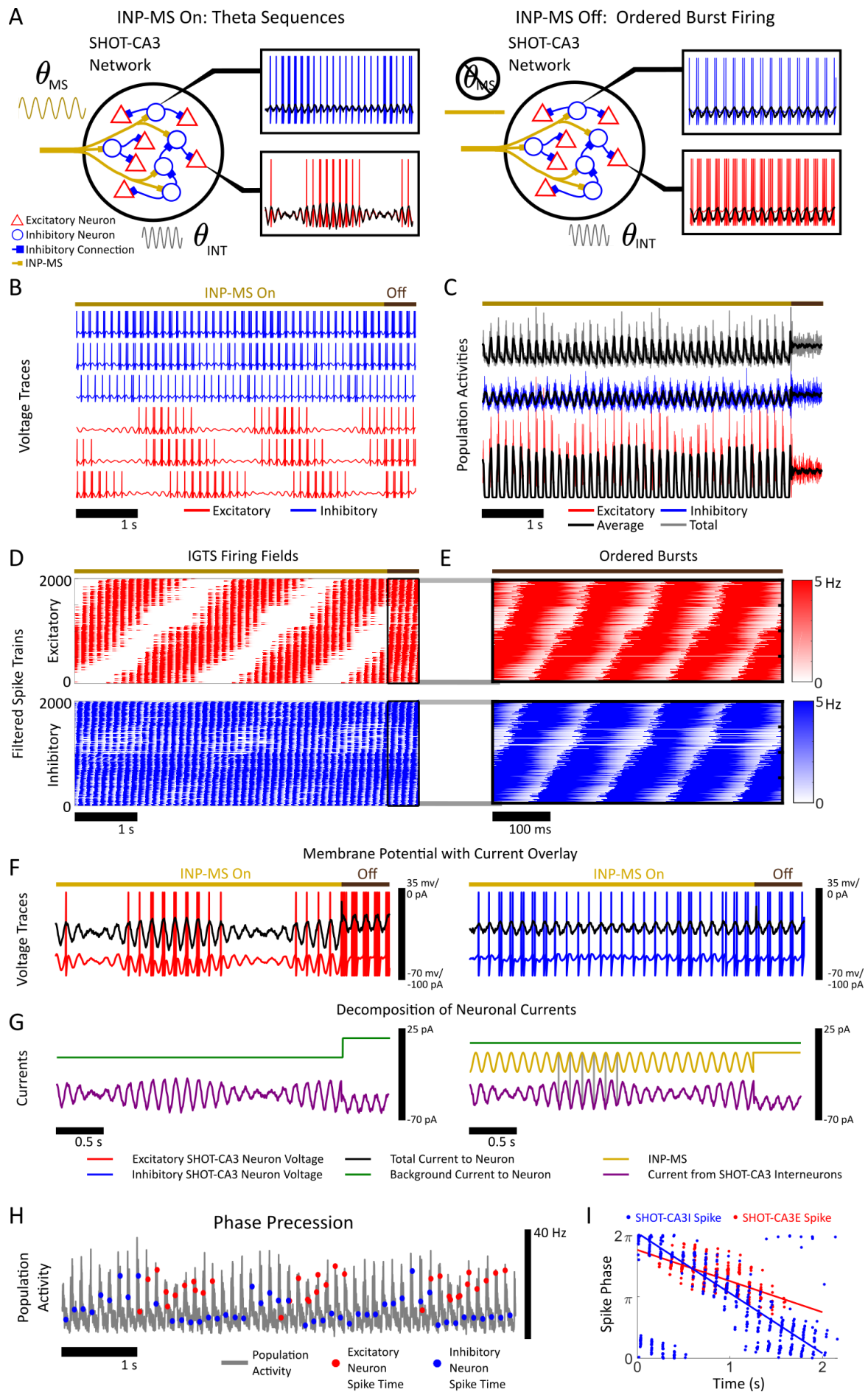
0   1   2

Time (s)

Figure 1

Figure 1: FORCE Training the SHOT-CA3 network

(A) Schematic of Septal-Hippocampal Oscillatory Theta, SHOT-CA3 network. (Left) When GABAergic inputs (gold) from INP-MS are present, firing fields emerge in SHOT-CA3E (red) while SHOT-CA3I (blue) fire theta-frequency bursts. (Right) When INP-MS is absent, all SHOT-CA3 neurons fire bursts. The SHOT-CA3I are trained to oscillate at a $\theta_{INT} = 8.5$ Hz frequency while receiving INP-MS oscillating at $\theta_{MS} = 8$ Hz. **(B)** The voltage traces for 3 excitatory neurons (red), 3 interneurons (blue). The overline denotes the presence (gold, first 5 s) or absence (brown, last 500 ms) of INP-MS. The result is an interference pattern generated due to these two oscillatory currents. **(C)** The population activities are computed as histograms by binning spikes over 1 ms bins for the excitatory (blue), inhibitory (red) and total (grey) populations in addition to the smoothed time averages (black, 20 ms box filter). The population activities oscillate at θ_{MS} in the presence of INP-MS. **(D)** The SHOT-CA3E are sequentially active (red) and have long timescale firing fields, while the SHOT-CA3I are sequentially active on the θ_{INT} timescale. The firing fields are plotted as synaptically filtered spike trains $\boldsymbol{r}(t)$ ($\tau_R = 2$ ms and $\tau_D = 20$ ms). Removal of INP-MS (last 500 ms) results in burst firing. **(E)** A zoomed-in segment consisting of 500 ms without INP-MS present. The order of compressed bursts is identical to the order of firing fields. **(F)** Voltage traces and total current (black) to an excitatory (red) and inhibitory (blue) SHOT-CA3 neuron. **(G)** Decomposition of the total current arriving to SHOT-CA3 excitatory neuron (left) and SHOT-CA3 interneuron (right) into background (green), synaptic (purple) and INP-MS (gold) sources. **(H)** Phase precessing spikes for an excitatory neuron (red points, spike times) and an interneuron (blue points, spike times) in the network in reference to total population activity (using $N = N_{CA3E} + N_{CA1I} = 4000$, grey) with INP-MS present. **(I)** The slope of phase precession for an excitatory neuron ($-0.51\pi/s$, $n = 22$ firing-fields) and an interneuron ($-0.97\pi/s$, $n = 22$ firing-fields).

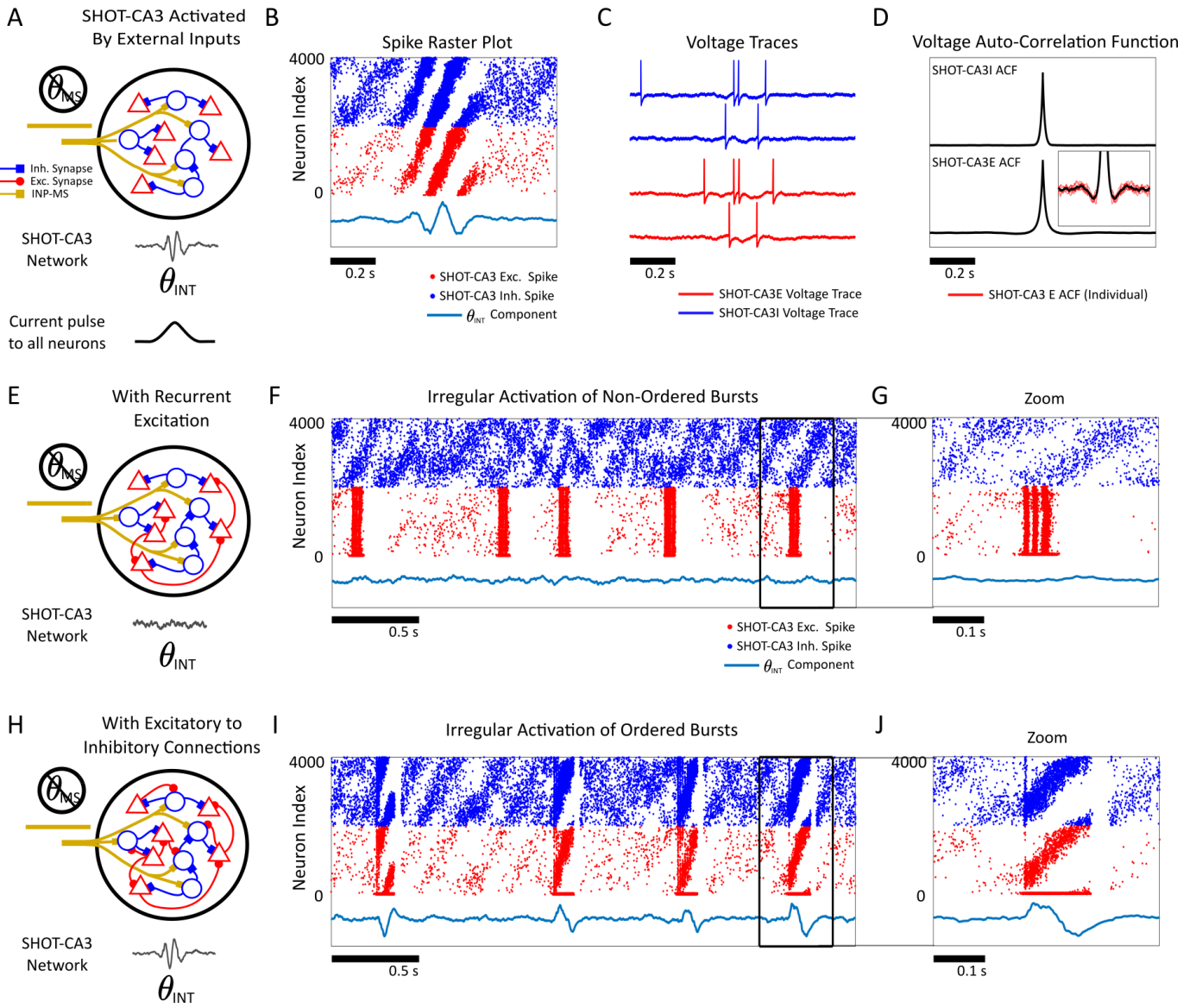# Irregular and Self Generated Activation of the Sharp Wave Oscillator

A SHOT-CA3 Activated By External Inputs

Inh. Synapse
Exc. Synapse
INP-MS

SHOT-CA3 Network

θ_{INT}

Current pulse to all neurons

B Spike Raster Plot

Neuron Index

0.2 s

• SHOT-CA3 Exc. Spike
• SHOT-CA3 Inh. Spike
— θ_{INT} Component

C Voltage Traces

0.2 s

— SHOT-CA3E Voltage Trace
— SHOT-CA3I Voltage Trace

D Voltage Auto-Correlation Function

SHOT-CA3I ACF

SHOT-CA3E ACF

0.2 s

— SHOT-CA3 E ACF (Individual)

E With Recurrent Excitation

SHOT-CA3 Network

θ_{INT}

F Irregular Activation of Non-Ordered Bursts

Neuron Index

0.5 s

• SHOT-CA3 Exc. Spike
• SHOT-CA3 Inh. Spike
— θ_{INT} Component

G Zoom

Neuron Index

0.1 s

H With Excitatory to Inhibitory Connections

SHOT-CA3 Network

θ_{INT}

I Irregular Activation of Ordered Bursts

Neuron Index

0.5 s

J Zoom

Neuron Index

0.1 s

Figure 2

15

Figure 2: Stochastically Initiating Sharp-Waves and Compressed Replay

(A) The SHOT-CA3E and SHOT-CA3I receive white noise to initiate spiking. A reduced background drive to SHOT-CA3I destroys the θ_{INT} oscillation. A pulse of current to all neurons transiently activates the θ_{INT} oscillator (FORCE component is shown in light blue). **(B)** The SHOT-CA3I (blue spike raster) and SHOT-CA3E (red spike raster) are driven by a Gaussian pulse current. This transiently activates θ_{INT} (reflected in FORCE component, light blue). **(C)** The voltage traces for SHOT-CA3I and SHOT-CA3E do not exhibit signs of θ_{INT}. **(D)** The voltage auto-correlations for the SHOT-CA3 neurons (red), SHOT-CA3I (blue) and the average of 20 neurons in each population for 1000 seconds of simulation with noise present. **(E)** The excitatory population now contains recurrent excitation. **(F)** A small sub-population of 50 neurons have dense recurrent coupling and projects to the rest of the population. This initiates stochastic synchronized bursting. The θ_{INT} oscillator is not activated by the excitatory coupling **(G)** A zoom of a synchronized burst triggered by recurrent excitation. **(H)** The recurrently coupled excitatory population now also projects to the inhibitory population to recruit the θ_{INT} oscillator transiently. **(I)** Ordered transient bursts are now initiated by the networks recurrence. **(J)** A zoom of the ordered burst generated by the recurrent excitation.
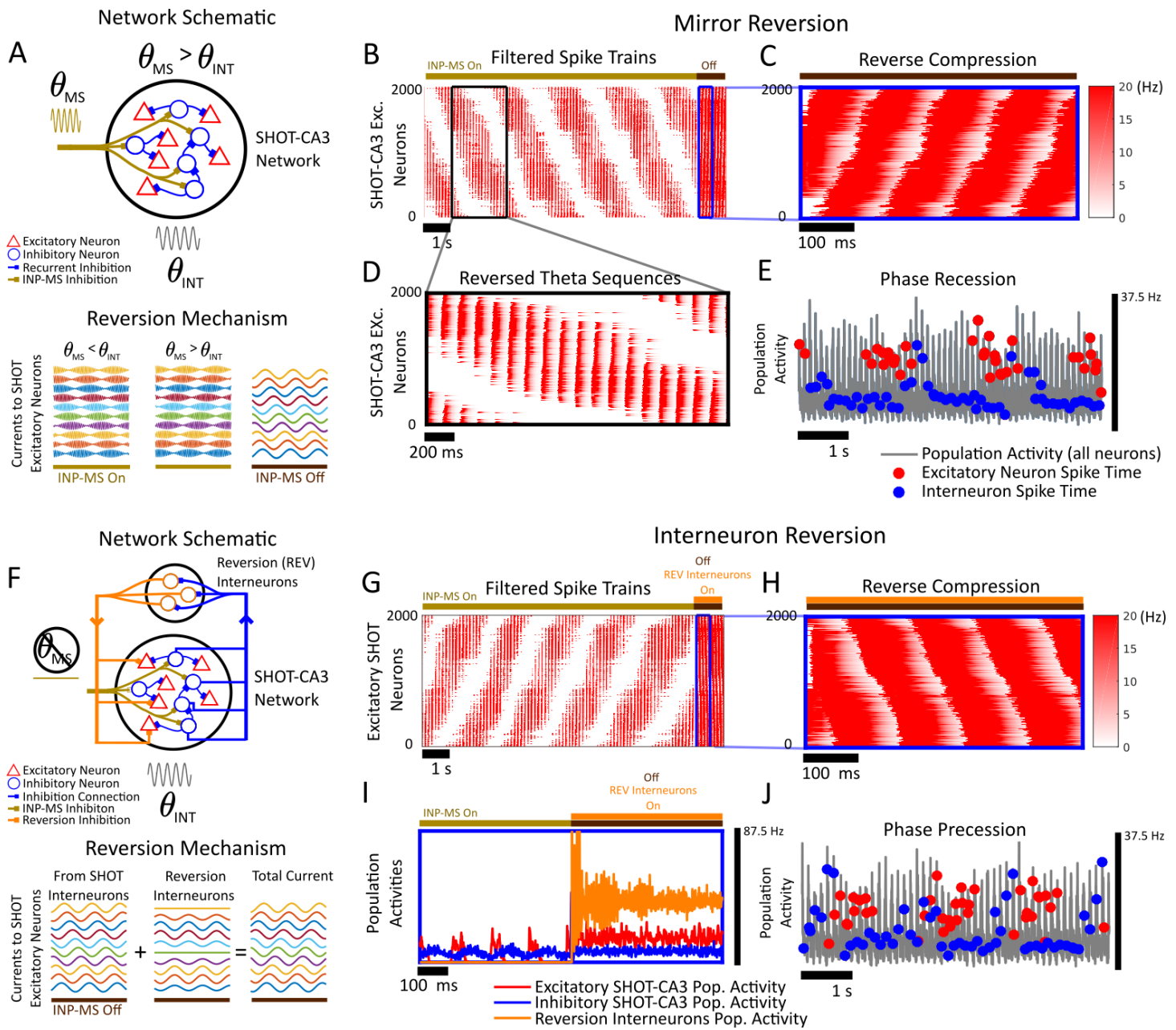
Figure 3

Figure 3: Two Mechanisms of Reverse Compression

(A) (Top) A SHOT-CA3 network schematic of reverse compression when the INP-MS frequency is faster than the recurrent oscillation ($\theta_{MS} > \theta_{INT}$). (Bottom) Schematic of the mathematical mechanism for mirror reversion. **(B)** The filtered spikes ($r(t)$, $\tau_D = 20$ ms, $\tau_R = 2$ ms) fired by the SHOT-CA3E. The overline denotes the presence (gold, first 10 seconds) or absence (brown, last 1 second) of INP-MS. **(C)** The zoomed 500 ms (highlighted in blue) segment in (B). The bursts occur in reverse order as in the firing fields from (B). **(D)** A zoomed-in segment of activity from (B). **(E)** Both excitatory (red dots, spike times) and interneurons (blue dots, spike times) recess in phase relative to the population activity (grey, average inhibitory recession rate $0.72\pi/s$, S.D. $0.37\pi/s$, $n = 100$, average excitatory rate, $0.4\pi/s$, S.D., $0.1\pi/s$, $n = 100$). **(F)** (Top) A network schematic of Interneuron Reversion, a reverse compression mechanism using a dedicated population of interneurons to trigger reverse compression. (Bottom) The mathematical mechanism that allows for this compression. The reversion interneurons first bursts of inhibition locked in time to θ_{INT}, with the burst rate varying as a function of the phase preference for the excitatory SHOT-CA3 neuron. **(G)** The firing fields are now in the same order as in Figure 1D. As in Figure 2(B), INP-MS is on for the first 10 seconds and deactivated for the final 1 second. The reversion interneurons are brought online when INP-MS is off. The overline's denote periods when INP-MS is present (gold), absent (brown), and when the reversion interneurons are turned on (orange). **(H)** A zoomed-in, 500 ms segment of reverse compression. The excitatory neurons fire bursts in reverse order relative to the firing fields. **(I)** The population activity for interneurons in SHOT-CA3 (blue), excitatory neurons in SHOT-CA3 (red) and the reversion interneurons (orange) for 500 ms before and 500 ms after INP-MS is removed. **(J)** Both excitatory (red dots, spike times) and interneurons (blue dots, spike times) precess in phase relative to the network theta-oscillation (grey) when the reversion interneurons are off. Phase precession rates are identical to Figure 1 (population activity using $N = N_{CA3E} + N_{CA1I} = 4000$, in grey).
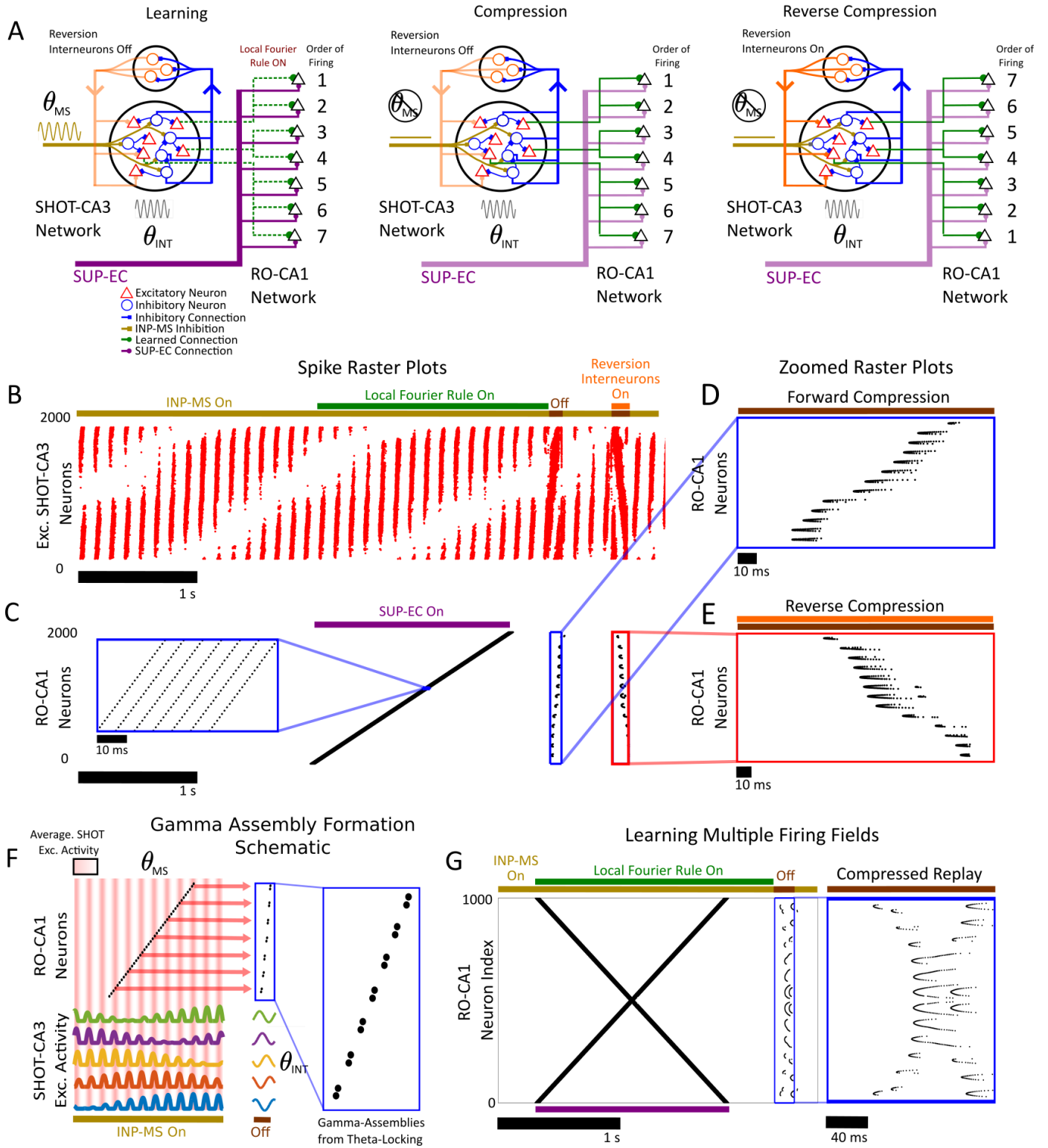
Learning Externally Evoked Spike Sequences

A Learning — Compression — Reverse Compression

B Spike Raster Plots

D Zoomed Raster Plots — Forward Compression

C

E Reverse Compression

F Gamma Assembly Formation Schematic

G Learning Multiple Firing Fields

Figure 4

Figure 4: Single-Trial Learning with a Septal-Hippocampal Oscillatory Theta Network

(A) Schematic of the network consisting of the SHOT-CA3 network (red for excitatory, blue for inhibitory), the reversion interneurons (orange), the RO-CA1 network (black). Inputs from the SUP-EC (purple) trigger the to-be-learned spike sequences in RO-CA1. (Left) In the learning phase, a set of feedforward weights are learned from SHOT-CA3 to the 2000 neurons in RO-CA1 using the local Fourier rule (connections in green) when INP-MS is on. The RO-CA1 neurons are activated in sequential order by external inputs (in purple). (Middle) In the replay phase, compressed and sequentially ordered bursts are triggered by removing INP-MS. (Right) Reverse compression can be elicited by activating the reversion interneurons simultaneously to removal of INP-MS. **(B)** The spike-raster plot for the excitatory neurons in the SHOT-CA3 network (red dots). The overlines denote the presence (gold) or absence (brown) of INP-MS, activation of the local Fourier rule (green), and activation of the reversion interneurons (orange). The INP-MS is on for the first 4 seconds during learning and is turned off twice ($t \in [4.015, 4.11], t \in [4.54, 4.675]$) with the reversion interneurons turned on for the second interval. **(C)** Spike-raster plot for the excitatory neurons in RO-CA1 (black dots). The purple overline denotes the presence of external inputs triggering sequential burst firing (inset in the left is a zoom). **(D)** A zoomed-in segment of compressed replay of the RO-CA1 neurons. The compressed replay takes the form of a sequence of high-frequency assemblies. **(E)** A zoomed-in segment of reverse compressed replay. **(F)** A schematic for the emergence of high-frequency assemblies from a combination of theta-phase segregation of spiking and the local Fourier rule. The activity in the SHOT-CA3E is segregated to specific phases in the theta oscillation which implies that spikes in RO-CA1 must fire spikes coincident with these phases for Hebbian learning. This creates assemblies during compression. **(G)** (Left) Similar as in (B), only with a different downstream spike sequence (X shape) where neurons have multiple firing fields. The INP-MS are turned off only once during $t \in [3.95, 4.11]$ to trigger a compressed replay. (Right) A zoomed-in segment of the compressed spike-replay when INP-MS is off. (B).
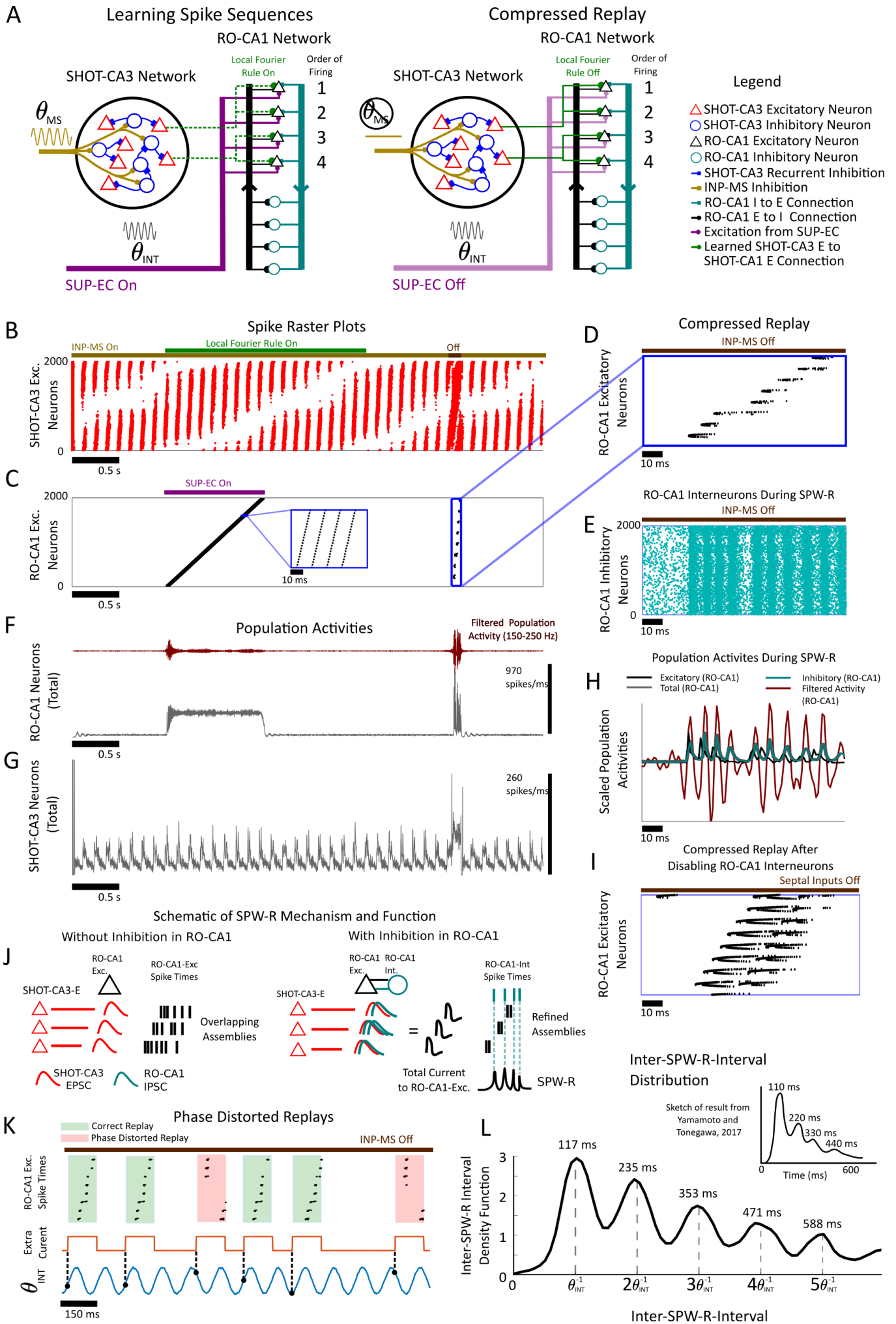
A

Learning Spike Sequences

RO-CA1 Network

SHOT-CA3 Network

Compressed Replay

RO-CA1 Network

SHOT-CA3 Network

Legend

△ SHOT-CA3 Excitatory Neuron
○ SHOT-CA3 Inhibitory Neuron
△ RO-CA1 Excitatory Neuron
○ RO-CA1 Inhibitory Neuron
▪ SHOT-CA3 Recurrent Inhibition
▪ INP-MS Inhibition
▪ RO-CA1 I to E Connection
• RO-CA1 E to I Connection
• Excitation from SUP-EC
• Learned SHOT-CA3 E to SHOT-CA1 E Connection

B Spike Raster Plots

C

D Compressed Replay

E RO-CA1 Interneurons During SPW-R

F Population Activities

G

H Population Activites During SPW-R

I Compressed Replay After Disabling RO-CA1 Interneurons

J Schematic of SPW-R Mechanism and Function

K Phase Distorted Replays

L Inter-SPW-R-Interval Distribution

Figure 5

21

Figure 5: Single-Trial Learning in Hippocampus

(A) Network schematic with SHOT-CA3 receiving INP-MS and a downstream RO-CA1 network. Inputs from SUP-EC (purple) trigger the to-be-learned spike sequences in RO-CA1. (Left) In the learning phase, SUP-EC inputs trigger sequential firing in RO-CA1E (black). The local Fourier rule binds the RO-CA1 spiking activity to the firing fields in the SHOT-CA3E (red). (Right) Compressed replay can be triggered after learning by turning off INP-MS. **(B)** The spike raster plot of SHOT-CA3E (red dots). The overlines denote the presence (gold) or absence (brown) of INP-MS, and the activation of the local Fourier rule (green). **(C)** The spike raster plot of RO-CA1E (black dots). The purple overline denotes the presence of inputs from SUP-EC. RO-CA1E are stimulated to fire bursts (see inset) by SUP-EC inputs during $t \in [1, 2]$. The INP-MS are turned off during $[4.03, 4.13]$ to trigger a compressed replay. **(D)** Zoom of compressed assembly replay triggered when INP-MS is off. **(E)** The spike raster plot for the RO-CA1Is (teal dots, time aligned with (D)). **(F)** The total population activity for the RO-CA1 (grey, time aligned with (B) and (C)). The band-pass (150-250 Hz) filtered population activity. **(G)** The total population activity in the SHOT-CA3 (grey). **(H)** A zoomed segment of the total RO-CA1 population activity (grey), the RO-CA1I population activity (teal), the RO-CA1E population activity (black), and the filtered ripple band (burgundy). Note that population activities have been normalized to have maximum activity set to unity, and are not to scale. High-frequency oscillations are triggered by the excitatory population. RO-CA1E high-frequency assemblies trigger the interneuron network to fire at a high frequency. **(I)** Compressed replay triggered by removing INP-MS while disabling the RO-CA1I. This causes the learned assemblies to overlap. **(J)** Schematic for sharp-wave-ripple formation and high-frequency-assembly refinement. The SHOT-CA3E trigger ordered but overlapping assembly spiking in RO-CA1 through their Excitatory Post Synaptic Potentials (EPSPs). When interneurons are included, the excitatory assemblies trigger the RO-CA1I to fire. The SHOT-CA3 EPSPs are refined in width by RO-CA1 IPSPs. **(K)** The INP-MS are kept off and sharp-wave-ripples are initiated by stochastically turning on an extra current (in orange) with a constant probability per unit time (see Materials and Methods). The learned connections from SHOT-CA3 to RO-CA1E are identical as in (B). Some replays are correct (green), while other replays are fragmented (red). One of the FORCE decoded θ_{INT} oscillators (light blue) demonstrates that correct replays are locked to the ascending component of the θ_{INT} oscillation while fragmented replays are locked to the descending phase of the θ_{INT} oscillation. We term this type of error phase distortion. **(L)** Phase distortion may be minimized by locking the probability of ripple initiation to the underlying θ_{INT} oscillation in the SHOT-CA3E. The inter-ripple-interval distribution (estimated after 3000 seconds of simulation) is a good qualitative match for the multi-modal distribution from [36] (top inset) which has peaks at the harmonics of a theta oscillation period of 110 ms although there are some quantitative errors as we use a slower θ_{INT}, $\theta_{INT}^{-1} = 150$ ms.

A

Wheel Running in the Two
Choice Alternating Reaction Task

Internally Generated Theta
Sequences in Hippocampus

θ_D
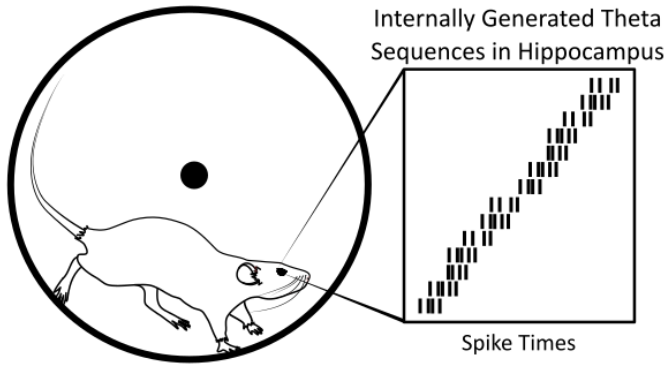
Optogenetic Frequency Driving
of the Medial Septum

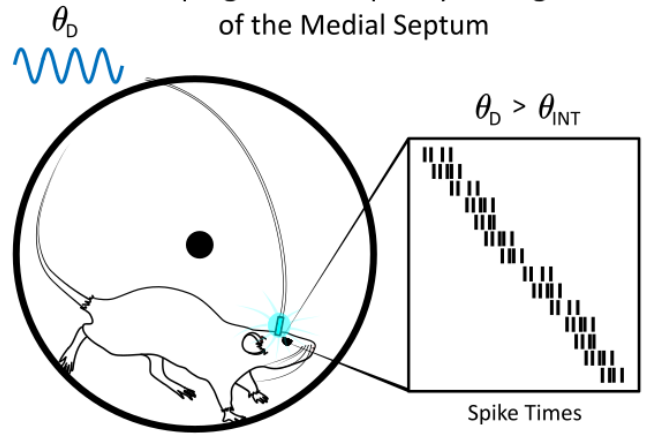$\theta_D > \theta_{INT}$

Spike Times

Spike Times

Figure 6

Figure 6: Experimental Predictions in Rodents

(A) Suggestion of a novel experiment to test our model of firing field formation. (Left) During the normal two choice alternating reaction task, ordered firing fields emerge during wheel running [6]. (Right) We suggest running the same task, only optogenetically stimulating interneurons in the medial septum with an oscillatory input of driving frequency of θ_D. The driving frequency θ_D is varied from wheel running trial to trial. When $\theta_D > \theta_{INT}$, the firing field orientation should reverse. Further, we predict that the resulting firing fields will display similar transitions as in our sweep protocol in Supplementary Figure 8.

4 Methods

Data Availability Statement

The data that support the findings in this study are available from the corresponding author upon request.

Code Availability Statement

The relevant code to generate the results of this paper can be found on modelDB [51], under accession number 243447.

4.1 Leaky Integrate and Fire Network

The Septal Hippocampal Oscillatory Theta (SHOT-CA3) network consists of coupled leaky integrate-and-fire neurons:

$$
\begin{aligned}
\tau_m \dot{v}_i^{CA3I} &= -v_i^{CA3I} + RI^{CA3I} + R \sum_{j=1}^{N_{CA3I}} \omega_{ij}^{CA3I,CA3I} r_j^{CA3I}(t) \\
&+ RI^{GABA}(\kappa + \cos(2\pi\theta_{MS}t)), \quad i = 1, 2, \ldots N_{CA3E} \quad (10)
\end{aligned}
$$

$$
\tau_m \dot{v}_i^{CA3E} = -v_i^{CA3E} + RI^{CA3E} + R \sum_{j=1}^{N_{CA3I}} \omega_{ij}^{CA3E,CA3I} r_j^{CA3I}(t) + RI_{syn,i}^{CA3E,REV}(t), \quad i = 1, 2, \ldots N_{CA3E} \quad (11)
$$

$$
\tau_m \dot{v}_i^{REV} = -v_i^{REV} + RI^{REV} + R \sum_{j=1}^{N_{CA3I}} \omega_{ij}^{REV,CA3I} r_j^{CA3I}(t), \quad i = 1, 2, \ldots N_{REV} \quad (12)
$$

where $CA3E, CA3I$ denote the excitatory and inhibitory populations of SHOT-CA3, respectively while REV denotes the reversion interneurons (see Materials and Methods Section 4.9). The neurons receive a constant background current I^α for $\alpha = CA3E, CA3I, REV$ current set at or above the threshold (see Table 1 for parameters). The parameter $R = 1 \cdot 10^9 \; \Omega$ serves as the resistance. When the voltage variables reach a threshold value, $v_{threshold}$, they are immediately reset to v_{reset} followed by an absolute refractory period, τ_{ref} during which the neuronal dynamics are quenched at the reset value. The membrane time constant, τ_m determines the degree to which the synaptic currents are filtered by the voltage dynamics. The spikes themselves are filtered by the double exponential synapse:

$$
\dot{r}_j^\alpha = -\frac{r_j^\alpha}{\tau_d} + h_j^\alpha \quad (13)
$$

$$
\dot{h}_j^\alpha = -\frac{h_j^\alpha}{\tau_r} + \frac{1 \cdot pA \cdot ms^2}{\tau_r \tau_d} \sum_{t_{jk} < t} \delta(t - t_{jk}) \quad (14)
$$

where τ_r is the synaptic rise time, and τ_d is the decay time t_{jk} is the kth spike fired by the jth neuron. The SHOT-CA3I all receive INP-MS where θ_{MS} is the input frequency, and $\kappa > 1$ determines the tonic level of inhibitory drive. The INP-MS has amplitude $I^{GABA} = -10$ pA for $i = 1, 2, \ldots N_I$. The excitatory neurons do not receive INP-MS. The reversion interneurons do not receive INP-MS (Figure 3-4) but our results still hold when the reversion interneurons receive INP-MS (Supplementary Figure 11). The network consists of $N_{CA3E} = N_{CA3I} = N_{REV} = 2000$ spiking neurons. However, the hippocampus is a circuit consisting of $O(10^5)$ neurons (in rat), and our network model of CA3 is not-to-scale. Thus, our results may not reflect the full behaviour of the much larger circuit.

The weight matrices $\boldsymbol{\omega}^{CA3I,CA3I}$, $\boldsymbol{\omega}^{CA3E,CA3I}$ are described in further detail in the section FORCE Training Internal Sequences. All weight matrices that we consider are unitless with the units of current (pA) carried by the synaptically filtered spike trains $r(t)$ (see Equation (14)). The SHOT-CA3E also receive a current from the reversion interneuron population (in Figures 2 and 4), $I_{syn}^{CA3E,REV}(t)$, which is described in greater detail in the section Reversion Interneuron Population. In all cases, when we refer to the filtered spike train, we mean $\boldsymbol{r}^\alpha(t)$ as given by Equation (13). However, the filtering time constants differ for different figures and different populations of neurons (see Table of Parameters). Note that the only connections in Equations (10)-(12) are from the SHOT-CA3I ($r^{CA3I}(t)$) or the reversion interneurons ($r^{REV}(t)$).

For Figure 4, the RO-CA1 layer was included in the simulation:

$$\tau_m \dot{v}_i^{CA1E} = -v_i^{CA1E} + RI^{CA1E} + R\sum_{j=1}^{N_E} \omega_{ij}^{CA1E,CA3E} r_j^{CA3E}(t) + RI_{syn,i}^{CA1,EC}(t) \tag{15}$$

where the weights $\omega_{ij}^{CA1E,CA3E}$ were trained using the local Fourier Rule. A series of external input currents $I_{syn}^{CA1,EC}(t)$ were transiently applied to elicit bursting. Further details are described in the supplementary notes.

Finally, we added another population of interneurons to RO-CA1 in Figure 5:

$$\tau_m \dot{v}_i^{CA1I} = -v_i^{CA1I} + RI^{CA1I} + R\sum_{j=1}^{N_{CA1E}} \omega_{ij}^{CA1I,CA1E} r_j^{CA1E}(t) + R\zeta_i(t), \quad i = 1,2,\ldots N_{CA1I}$$

$$\tau_m \dot{v}_i^{CA1E} = -v_i^{CA1E} + RI^{CA1E} + R\sum_{j=1}^{N_{CA1I}} \omega_{ij}^{CA1E,CA1I} r_j^{CA1I}(t)$$

$$+ R\sum_{j=1}^{N_{CA3E}} \omega_{ij}^{CA1E,CA3E} r_j^{CA3E}(t) + RI_{syn,i}^{CA1E,EC}(t), \quad i = 1,2,\ldots N_{CA1E}$$

where $\zeta_i(t)$ is an independent white noise term with mean 0 and standard deviation $\sigma = 0.2$ pA. This noise term was added to the interneurons to prevent pathological synchrony in the RO-CA1Is. The weight matrices $\boldsymbol{\omega}^{CA1E,CA1I}$, $\boldsymbol{\omega}^{CA1E,CA1I}$ are untrained and discussed further in the section Further Methods for Figure 5. The inputs from the entorhinal cortex to the RO-CA1Es, $I_i^{CA1E,EC}(t)$ are also described in the section Further Methods for Figure 5. Finally, the weight matrix $\boldsymbol{\omega}^{CA1E,CA3E}$ is trained by the local Fourier rule, which is discussed further in the Supplementary Materials Section S1. Finally, we note that the synaptic currents from SHOT-CA3I, $I_{syn}^{CA3E,CA3I}(t), I_{syn}^{CA3I,CA3I}(t)$, display characteristics of an interference pattern between θ_{INT} and θ_{MS} oscillations. These currents can be non-dimensionalized as follows:

$$I_{i,syn}^{CA3E,CA3I}(t) = b_i^1 z_i(t) + b_i^0 \tag{16}$$

$$z_i(t) \approx \cos(2\pi\theta_{MS}t) + \cos(2\pi\theta_{INT}t + \psi_i) \tag{17}$$

where b_i^1 carries the amplitude (and dimensions) of the current, b_i^0 carries the baseline amount, and $z_i(t)$ is the fluctuating component that displays the interference between oscillations. We consider all analytical derivations on the dimensionless current, $z_i(t)$. The parameters b_i^1 and b_i^0 are auxiliary-parameters in the subsequent derivations and need not be explicitly computed.

4.2 FORCE Training Inhibitory Connections in a Balanced E/I Network

The weight matrices $\boldsymbol{\omega}^{\alpha\beta} = \boldsymbol{S}^{\alpha\beta} + \boldsymbol{L}^{\alpha\beta}$, $\alpha, \beta = CA3E, CA3I$ are decomposed into static terms ($\boldsymbol{S}^{\alpha\beta}$) that are chosen to form an initial balanced spiking network, and learned terms ($\boldsymbol{L}^{\alpha\beta}$) that are FORCE trained [8]. The static term is given by:

$$\boldsymbol{S}_{ij}^{\alpha\beta} = \begin{cases} \frac{\gamma \cdot g}{\sqrt{pN_\beta}} \iota_{ij}^{\alpha\beta} & \beta = CA3E \\ -\frac{g}{\sqrt{pN_\beta}} \iota_{ij}^{\alpha\beta} & \beta = CA3I \end{cases} \tag{18}$$

With N_{CA3E} excitatory neurons and N_{CA3I} interneurons, each neuron receives precisely $C_{CA3E} = pN_{CA3E}$ excitatory connections and $C_{CA3I} = pN_{CA3I}$ inhibitory connections from the rest of the network where p is the degree of sparsity in the network. The variable $\iota_{ij}^{\alpha\beta} = 1$ if a connection is present between neuron j in population β (presynaptic) and neuron i in population α (postsynaptic), and 0 otherwise. The variable g controls the coupling strength while $\gamma = \sqrt{C_{CA3I}/C_{CA3E}}$ is used to balance the weight matrix in cases where $C_{CA3I} \neq C_{CA3E}$. Here however, we do not train a balanced E/I network, but rather a balanced I network (see Materials and Methods: FORCE Training a Balanced I Network) [54]. We include this section for completion.

In normal FORCE training, the learned term is given by the following:

$$L_{ij}^{\alpha\beta} = q\left(\boldsymbol{\eta}_i^\alpha \cdot \boldsymbol{\phi}_j^\beta\right) \tag{19}$$

where q determines the amount of learned recurrence the network receives and $\boldsymbol{\eta}_i^\alpha$ and $\boldsymbol{\phi}_j^\beta$ are referred to as the neural encoders and decoders, respectively [8]. The encoders help determine the tuning preferences of the

neurons. The decoders are trained using Recursive Least Squares (RLS), an online L_2 minimization scheme described in further detail in the section Recursive Least Squares. The network approximant of the intended dynamics is given by the following

$$\hat{x}(t) = \phi^T \begin{pmatrix} r^{CA3E}(t) \\ r^{CA3I}(t) \end{pmatrix} \tag{20}$$

Here we want to pre-specify which neuron is excitatory and which is inhibitory (although that would not be necessary for hippocampus [3]). To that end, it is sufficient (but not necessary) to constrain the learned component of the weight matrix:

$$L_{ij}^{\alpha\beta} = \begin{cases} q|\boldsymbol{\eta}_i^\alpha \cdot \boldsymbol{\phi}_j^\beta|, & \beta = CA3E, \quad \boldsymbol{\eta}_i^\alpha \cdot \boldsymbol{\phi}_j^\beta > 0 \\ -q|\boldsymbol{\eta}_i^\alpha \cdot \boldsymbol{\phi}_j^\beta|, & \beta = CA3I, \quad \boldsymbol{\eta}_i^\alpha \cdot \boldsymbol{\phi}_j^\beta < 0 \\ 0 & \text{otherwise} \end{cases} \tag{21}$$

While implementing the boundary condition (Equation (21)) on $L_{ij}^{\alpha\beta}$ is sufficient, it is time consuming during learning as it requires $O(N^2)$ computations to bound every weight in the weight matrix. We opt to impose a condition on the encoders and decoders separately. Consider the following operations:

$$(s)_+ = \begin{cases} s, & s \geq 0 \\ 0 & s < 0 \end{cases}, \quad (s)_- = \begin{cases} s, & s \leq 0 \\ 0 & s > 0 \end{cases} \tag{22}$$

where the operation $(s)_\pm$ sets s to 0 if its negative (positive) and retains its value otherwise.

First, we decompose the decoders and encoders as follows:

$$
\begin{aligned}
\boldsymbol{\eta}_i^\alpha \cdot \boldsymbol{\phi}_j^\beta &= \left((\boldsymbol{\eta}_i^\alpha)_+ + (\boldsymbol{\eta}_i^\alpha)_- \right) \cdot \left(\left(\boldsymbol{\phi}_j^\beta \right)_+ + \left(\boldsymbol{\phi}_j^\beta \right)_- \right) \\
&= (\boldsymbol{\eta}_i^\alpha)_+ \cdot \left(\boldsymbol{\phi}_j^\beta \right)_+ + (\boldsymbol{\eta}_i^\alpha)_+ \cdot \left(\boldsymbol{\phi}_j^\beta \right)_- + (\boldsymbol{\eta}_i^\alpha)_- \cdot \left(\boldsymbol{\phi}_j^\beta \right)_+ + (\boldsymbol{\eta}_i^\alpha)_- \cdot \left(\boldsymbol{\phi}_j^\beta \right)_- \\
&= (\boldsymbol{\eta}_i^\alpha)_+ \cdot \left(\boldsymbol{\phi}_j^\beta \right)_+ + (\boldsymbol{\eta}_i^\alpha)_- \cdot \left(\boldsymbol{\phi}_j^\beta \right)_- \\
&\quad + (\boldsymbol{\eta}_i^\alpha)_+ \cdot \left(\boldsymbol{\phi}_j^\beta \right)_- + (\boldsymbol{\eta}_i^\alpha)_- \cdot \left(\boldsymbol{\phi}_j^\beta \right)_+
\end{aligned}
$$
$$\tag{23}$$
$$\tag{24}$$

Note that the terms on line (23) are positive while the terms on line (24) are negative. Thus, we can consider the following weights

$$L_{ij}^{\alpha\beta} = \begin{cases} (\boldsymbol{\eta}_i^\alpha)_+ \cdot \left(\boldsymbol{\phi}_j^\beta \right)_+ + (\boldsymbol{\eta}_i^\alpha)_- \cdot \left(\boldsymbol{\phi}_j^\beta \right)_- & \beta = CA3E \\ (\boldsymbol{\eta}_i^\alpha)_+ \cdot \left(\boldsymbol{\phi}_j^\beta \right)_- + (\boldsymbol{\eta}_i^\alpha)_- \cdot \left(\boldsymbol{\phi}_j^\beta \right)_+ & \beta = CA3I \end{cases} \tag{25}$$

which implements an alternate boundary condition to (21). Furthermore, implementing (25) only requires $O(N)$ computations as only encoders and decoders are bounded by their signs. This derivation, among other results, is originally owed to [52].

4.3 Recursive Least Squares

The decoders are determined dynamically to minimize the squared error between the approximant and intended dynamics, $\boldsymbol{e}(t) = \hat{\boldsymbol{x}}(t) - \boldsymbol{x}(t)$. The Recursive Least Squares (RLS) technique updates the decoders accordingly:

$$
\begin{aligned}
\phi(t) &= \phi(t - \Delta t) - \frac{\boldsymbol{e}(t)\boldsymbol{P}(t - \Delta t)\boldsymbol{r}(t)}{1 + \boldsymbol{r}(t)^T \boldsymbol{P}(t - \Delta t)\boldsymbol{r}(t)} \\
\boldsymbol{P}(t) &= \boldsymbol{P}(t - \Delta t) - \frac{\boldsymbol{P}(t - \Delta t)\boldsymbol{r}(t)\boldsymbol{r}(t)^T \boldsymbol{P}(t - \Delta t)}{1 + \boldsymbol{r}(t)^T \boldsymbol{P}(t - \Delta t)\boldsymbol{r}(t)}
\end{aligned}
$$
$$\tag{26}$$
$$\tag{27}$$

and $\boldsymbol{r}(t) = (\boldsymbol{r}^{CA3E}(t), \boldsymbol{r}^{CA3I}(t))^T$. RLS and FORCE training is described in greater detail in [8, 53]. The network is initialized with $\phi(0) = \mathbf{0}$, $\boldsymbol{P}(0) = \boldsymbol{I}_N \mu^{-1}$, where $\boldsymbol{I}_N$ is an N-dimensional identity matrix, and μ controls the learning rate of RLS.

4.4 FORCE Training a Balanced I Network

In addition to the procedure described above, a balanced network can be generated with recurrent inhibition alone [54]. In particular, we can consider the same network equations as before with the constraints:

$$S_{ij}^{CA3E,CA3E} = 0, \quad S_{ij}^{CA3I,CA3E} = 0,$$
$$I^{CA3I} = I_{threshold} + O(\sqrt{pN_{CA3I}})$$
$$I^{CA3E} = I_{threshold} + O(\sqrt{pN_{CA3I}})$$

where the interneuron network receives a super-threshold $I^{CA3I} > I_{threshold} = -40$ pA background current that is being balanced by the recurrent inhibition. The excitatory neurons in the population also receive inhibitory connections and thus have a super-threshold background current after FORCE training is concluded. However, during FORCE training, the current I^{CA3E} is clamped to below the threshold ($I^{CA3E} < I_{threshold}$) to prevent firing in the excitatory neurons thereby eliminating both EE and IE weights. This occurs through the dependence of Equation (26) on $\boldsymbol{r}^{CA3E}(t)$, and $\boldsymbol{\phi}(0) = 0$.

4.5 Internally Generated Theta Sequence

To construct a SHOT-CA3 network with a recurrently generated theta sequence of firing, we FORCE train the network to learn the following supervisor:

$$\boldsymbol{x}_i(t) = \cos(2\pi\theta_{INT}t + \chi_i), \quad i = 1, 2, \ldots, m \tag{28}$$

Here, θ_{INT} is the frequency of the oscillation that is embedded in the recurrent weights of the network and χ_i is a phase shift for the m components of the supervisor. The m components of the supervisor yield an $N \times m$ dimensional matrix of encoders and decoders with $m = 100$ components. For each neuron, exactly one encoder element is non-zero and is set to 1. The phase shift is randomly selected and uniformly distributed over $[0, 2\pi]$. When trained in this fashion, the inhibitory currents and INP-MS combine to generate an interference pattern in the excitatory neurons (see Supplementary Figure 1-2):

$$z_i(t) \approx \cos(2\pi\theta_{MS}t) + \cos(2\pi\theta_{INT}t + \psi_i), \quad i = 1, 2, \ldots N_{CA3E} \tag{29}$$

We interpret $z_i(t)$ to be the fluctuating, dimensionless, component of the current an excitatory SHOT-CA3 neuron receives. Note that we have written ψ_i as opposed to χ_i as the phases of the excitatory neurons are only indirectly related to the phases in the supervisor (Equation (28)). This is due to the operations applied in Equation (25).

4.6 Interference Based Control of the Population Activity by INP-MS

With the currents arriving at each neuron given by Equation (29), we consider the conditions under which INP-MS influences the population activity of SHOT-CA3. In particular, we will set out to provide sufficient conditions under which the population activity $\rho(t)$ is a periodic function in time with period θ_{MS}^{-1}. Proceeding generally, we assume that a network transforms its currents via some unspecified differentiable non-linearity $F(z)$ where $F(z) \geq 0$ into spike rates. This implies that the population activity is given by the following:

$$\rho(t) = \int_0^{2\pi} \rho_\psi(\psi)F\left[\cos(2\pi\theta_{INT}t + \psi) + \cos(2\pi\theta_{MS}t)\right] d\psi \tag{30}$$

The function $\rho(t)$ is the population activity for a network of neurons with identical tuning curves $F(z)$ receiving heterogeneous currents, $z_i(t)$. The heterogeneity is in the phases of the currents, $z_i(t)$ through the variable $\tilde{\psi}_i$. We assume that this parameter comes from a static distribution with density function $\rho_\psi(\psi)$. Now, consider $\rho(t + \theta_{MS}^{-1})$:

$$\rho(t + \theta_{MS}^{-1}) = \int_0^{2\pi} \rho_\psi(\psi)F\left[\cos(2\pi\theta_{INT}\left(t + \theta_{MS}^{-1}\right) + \psi) + \cos(2\pi\theta_{MS}(t + \theta_{MS}^{-1}))\right] d\psi \tag{31}$$

$$= \int_0^{2\pi} \rho_\psi(\psi)F\left[\cos(2\pi\theta_{INT}t + \psi + 2\pi\theta_{INT}\theta_{MS}^{-1}) + \cos(2\pi\theta_{MS}t)\right] d\psi \tag{32}$$

$$= \int_{2\pi\theta_{INT}\theta_{MS}^{-1}}^{2\pi+2\pi\theta_{INT}\theta_{MS}^{-1}} \rho_\psi(\omega - 2\pi\theta_{INT}\theta_{MS}^{-1})F\left[\cos(2\pi\theta_{INT}t + \omega) + \cos(2\pi\theta_{MS}t)\right] d\omega \tag{33}$$

If the phase distribution is uniform ($\rho_\psi(\psi) = \frac{1}{2\pi}$), then:

$$
\begin{aligned}
\rho(t + \theta_{MS}^{-1}) &= \int_{2\pi\theta_{INT}\theta_{MS}^{-1}}^{2\pi+2\pi\theta_{INT}\theta_{MS}^{-1}} \frac{1}{2\pi} F\left[\cos(2\pi\theta_{INT}t + \omega) + \cos(2\pi\theta_{MS}t)\right] d\omega \qquad (34)\\
&= \int_0^{2\pi} \frac{1}{2\pi} F\left[\cos(2\pi\theta_{INT}t + \omega) + \cos(2\pi\theta_{MS}t)\right] d\omega \qquad (35)\\
&= \rho(t) \qquad (36)
\end{aligned}
$$

where line (35) is justified by the fact that $G(\omega, t) = F\left[\cos(2\pi\theta_{INT}t + \omega) + \cos(2\pi\theta_{MS}t)\right]$ is periodic in ω with period 2π and phase shifts ($2\pi\theta_{INT}\theta_{MS}^{-1}$ in line (34)) do not alter integrals of periodic functions. This implies that a uniform distribution is a sufficient condition for θ_{MS} control of population activities. Finally, we consider $\rho(t)$ when INP-MS is removed:

$$
\begin{aligned}
\rho(t) &= \int_0^{2\pi} \rho_\psi(\psi) F\left[\cos(2\pi\theta_{INT}t + \psi)\right] d\psi \\
\dot\rho(t) &= -2\pi\theta_{INT} \int_0^{2\pi} \rho_\psi(\psi) F_z\left[\cos(2\pi\theta_{INT}t + \psi)\right] \sin(2\pi\theta_{INT} + \psi_i) \, d\psi
\end{aligned}
$$

where F_z denotes the derivative of the function $F(z)$, $F'(z)$. If we again assume that ψ is uniformly distributed, then we arrive at the following:

$$
\begin{aligned}
\dot\rho(t) &= -\theta_{INT} \int_0^{2\pi} F_z\left[\cos(2\pi\theta_{INT}t + \psi)\right] \sin(2\pi\theta_{INT}t + \psi) \, d\psi \\
&= \left. \frac{1}{2\pi} F\left[\cos(2\pi\theta_{INT}t + \psi)\right] \right|_0^{2\pi} = 0
\end{aligned}
$$

and thus $\rho(t)$ is a constant and given by $\rho(t) = \rho(0) = \frac{1}{2\pi} \int_0^{2\pi} F(\cos(\psi)) d\psi$. Thus for uniformly distributed phase preferences, the population activity is constant in the absence of INP-MS despite the fact that all the neurons are oscillating.

4.7   Interference Based SPW-R and Theta Phase Compression of Spike Sequences

Multiple-oscillator models are well studied in the literature [9, 10, 55, 56]. However, here we demonstrate that reversible sharp-wave ripple compression is also well explained by interference theory, and that the phase precession based compression and sharp-wave based compression share the same mechanism in interference theory. Considering the current arriving at the SHOT-CA3E, $z_i(t)$, again,

$$
\begin{aligned}
z_i(t) &= \cos(2\pi\theta_{MS}t) + \cos(2\pi\theta_{INT}t + \psi_i) \qquad (37)\\
&= 2\underbrace{\cos\left(2\pi t \left(\frac{\theta_{MS} + \theta_{INT}}{2}\right) + \frac{\psi_i}{2}\right)}_{C(t),\ \text{Carrier}} \underbrace{\cos\left(2\pi t \left(\frac{\theta_{MS} - \theta_{INT}}{2}\right) - \frac{\psi_i}{2}\right)}_{E(t),\ \text{Envelope}} \qquad (38)
\end{aligned}
$$

Equation (38) implies that the firing field order is controlled by the envelope $\cos\left(2\pi t \left(\frac{\theta_{MS} - \theta_{INT}}{2}\right) - \frac{\psi_i}{2}\right)$ and in particular the phases $\frac{\psi_i}{2}$. If the phase distribution of ψ_i is uniform, then the firing-fields are uniformly distributed in time. If $\theta_{MS} < \theta_{INT}$ then the envelopes have phases $\psi_i/2$, while if $\theta_{MS} > \theta_{INT}$ the phases become reversed with $-\psi_i/2$. The end effect of this transformation is to either preserve or reverse the order of the firing fields (the envelope).

4.8   Reverse Compressed Replay with Dual Oscillator Based Mechanisms

If INP-MS is removed, the interference pattern collapses and the neurons receive the input

$$
z_i^{FOR}(t) = \cos(2\pi\theta_{INT}t + \psi_i) \qquad (39)
$$

where FOR is short for forward compression. Removal of INP-MS triggers a compression provided that the neurons also receive an additional super-threshold constant current. Thus, the default compression mode is a

forward compression, where bursts occur in the same order as the firing-fields when INP-MS is present. This compression can be reversed in two ways: 1) reverse the order of the firing fields $z_i(t)$ and maintain $z_i^{FOR}(t)$ or 2) reverse $z_i^{FOR}(t)$ and maintain the order of firing fields.

In mirror reversion, INP-MS is present and satisfies the frequency relationship $\theta_{MS} > \theta_{INT}$. The firing fields are reversed in order relative to the compression phase. However, this is not a valid mechanism for reverse compression as $\theta_{MS} > \theta_{INT}$, both excitatory and interneuron populations recess in phase. To our knowledge, phase recession has only been observed once [19]. In harmonic reversion, the firing-fields reverse near harmonics of θ_{INT} (see Supplementary Figure 8). For θ_{MS} just slightly larger than $\theta_{INT}/2$, the firing fields reverse and display phase precession instead of phase recession.

Finally, directly reversing $z_i^{FOR}(t)$ also triggers a reverse compressed replay. An additional population of interneurons, the reversion interneurons, is sufficient for this type of reversion. Reverse compression corresponds to SHOT-CA3E receiving the current:

$$
\begin{aligned}
z_i^{REV}(t) &= \cos(2\pi\theta_{INT}t - \psi_i) \\
&= \cos(2\pi\theta_{INT}t + \psi_i) + (\cos(2\pi\theta_{INT}t - \psi_i) - \cos(2\pi\theta_{INT}t + \psi_i)) \\
&= \cos(2\pi\theta_{INT}t + \psi_i) + 2\sin(\psi_i)\sin(2\pi\theta_{INT}t) \\
&= z_i^{FOR}(t) + 2\sin(\psi_i)\sin(2\pi\theta_{INT}t) \\
&= z_i^{FOR}(t) + AMP(\psi_i)\sin(2\pi\theta_{INT}t)
\end{aligned}
$$

Thus, reversion interneurons should be inhibited by SHOT-CA3I (through $\sin(2\pi\theta_{INT}t)$) while subsequently inhibiting the excitatory neurons. The amount of inhibition an excitatory neuron in SHOT-CA3 receives from the reversion population is controlled by the amplitude function $AMP(\psi_i) = 2\sin(\tilde{\psi}_i)$.

4.9 Reversion Interneuron Population

The reversion population is a population of N_{REV} interneurons with LIF dynamics that receives inhibition from SHOT-CA3I. For simplicity, we take $N_{REV} = N_{CA3I}$ and $\boldsymbol{\omega}^{REV,CA3I} = -\omega^{REV,CA3I}\boldsymbol{I}_{N_{CA3I}}$, where $\boldsymbol{I}_{N_{CA3I}}$ is the $N_{CA3I} \times N_{CA3I}$ identity matrix and $\omega^{REV,CA3I}$ is a scalar quantity with ($\omega^{REV,CA3I} = 1$) that determines the amount of inhibition the reversion population receives. The only parameter difference between the reversion population and the other neurons is the background current, I^{REV}, which varies when INP-MS is present or absent (see Figure 3, Figure 4 Captions).

From the preceding section, we require the reversion population to transmit the signal $2\sin(\psi_i)\sin(2\pi\theta_{INT}t)$ in a biologically plausible manner. First, the reversion interneurons must be locked into the internally generated theta oscillation through the term $\sin(2\pi\theta_{INT}t)$. Thus, we train a decoder $\boldsymbol{\phi}^{REV}$ that can decode $\sin(2\pi\theta_{INT}t)$ from the activity of the reversion population:

$$
\hat{s}(t) = (\boldsymbol{\phi_{REV}})^T \boldsymbol{r}^{REV}(t) \approx \sin(2\pi\theta_{INT}t) = s(t) \tag{40}
$$

where $\boldsymbol{\phi_{REV}}$ is trained using the decoded internal oscillators of the SHOT-CA3 network as a supervisor. The training is not performed online as in RLS but is learned immediately through L_2 optimization:

$$
\phi_{REV} = \left(\int_0^T \boldsymbol{r}_{REV}(t)\boldsymbol{r}_{REV}(t)^T + I_{N_{REV}}\delta \right)^{-1} \left(\int_0^T \boldsymbol{r}_{REV}(t)s(t)^T \right) dt \tag{41}
$$

where $\delta = 50$ acts as a regularization parameter and $T = 25$ s was used to compute ϕ^{REV}. Finally note that the current:

$$
I_{syn,i}^{CA3E,REV}(t) = -A^{REV}(2 - 2\sin(\psi_i)\hat{s}(t)) < 0 \tag{42}
$$

is strictly inhibitory and performs the necessary reversion in the excitatory neurons. The parameter A^{REV} is used to scale the current upward so that the SHOT-CA3 interneuron and reversion interneuron currents are of similar magnitude ($A^{REV} = 10$ pA). As the excitatory neurons receive an extra source of inhibition, they require a larger excitatory drive when INP-MS is deactivated. Further, as the current $I_{syn,i}^{CA3E,REV}(t)$ is strictly negative, a set of weights $\boldsymbol{\omega}^{CA3E,REV}$ can be found by a constrained optimization problem

$$
\text{argmin}_{\boldsymbol{\omega}^{CA3E,REV}} \|\boldsymbol{\omega}^{CA3E,REV}\boldsymbol{r}^{REV}(t) - \boldsymbol{I}_{syn}^{CA3E,REV}(t)\|^2 \quad \boldsymbol{\omega}_{ij}^{CA3E,REV} \leq 0, \quad \forall i,j
$$

This problem can be solved numerically for example with the MATLAB function lsqnonneg. However, for simplicity, we do not take this approach and simply apply the negative current (42) to the SHOT-CA3E.

4.10   High Frequency Assembly Frequency as a Function of θ_{INT} and θ_{MS}

Here, we will derive the relationship between, θ_{MS}, the interneuron recurrent oscillation frequency, θ_{INT}, and the high-frequency assemblies during compressed replay (without INP-MS). We refer to the frequency of these assemblies as Γ. As in experimental data, these assemblies nest on both theta and SPW states [30–32, 57–59]

The quantity n_x denotes the number of cycles of the oscillation x (either $x = MS$ or $x = INT$) in a specific time period while $\tau_{MS} = \theta_{MS}^{-1}$, $\tau_{INT} = \theta_{INT}^{-1}$, and $\tau = (\theta_{INT} - \theta_{MS})^{-1}$ is the period of the firing field. First, as the number of theta cycles (θ_{MS}), determines the number of assemblies (Figure 5F), then the total number of theta cycles is

$$n_\Gamma = n_\theta = \frac{\tau}{\tau_{MS}} = \frac{\theta_{MS}}{\theta_{INT} - \theta_{MS}} \tag{43}$$

then the frequency of assemblies during SPW-R compression, which we define as $\Gamma = \frac{n_\Gamma}{\tau_{INT}}$ is given by

$$\Gamma = \frac{n_\Gamma}{\tau_{INT}} = \frac{\theta_{INT} \cdot \theta_{MS}}{\theta_{INT} - \theta_{MS}} \tag{44}$$

As our analysis in the Methods section Interference Based Control of the Population Activity by INP-MS demonstrates, we only observe θ_{MS} in the population activity or other aggregate/macroscopic metrics. Thus, it is useful to write $\theta_{INT} = \theta_{MS} + \epsilon$, $\epsilon = \frac{1}{\tau}$, and thus:

$$\Gamma = \epsilon^{-1}(\theta_{MS} + \epsilon)\theta_{MS} = \theta_{MS} + \frac{\theta_{MS}^2}{\epsilon} \tag{45}$$

which in our case yields $\epsilon = 0.5$ Hz, $\theta_{MS} = 8$ Hz, yields an assembly frequency of $\Gamma = 136$ Hz. This is in good agreement with the results of Figure 4 and Figure 5. In Figure 4, we see 13 assemblies over an 88 ms interval, yielding $\Gamma \approx 147.7$ Hz (forward replay), 13 assemblies over 98 ms, yielding $\Gamma \approx 132.65$ (reverse replay), while in Figure 5 we see 8 assemblies over a 70 ms interval yielding $\Gamma \approx 114$ Hz.

4.11   Statistical Methods

Due to the deterministic nature of the model, the only statistical tests performed in this manuscript were in Supplementary Figure 9, to determine if network responses to current or amplitude ramps were non-zero.

An F-test was used in all cases, as implemented in the MATLAB fitlm model. All residuals were assumed to be normal, although this was not formally tested. For small current ramps, the data in Supplementary Figure 9 showed some skewness inconsistent with normality. We opted not to exclude this data as this effect vanishes for larger values of I^{CA3I}. Additionally, some of the data tested in Supplementary Figure 9 displayed a minor amount of nonlinearity, inconsistent with a linear regression assumption. However, we opted for a simple first order (linear fit), rather than more elaborate methods. No statistical methods were used to pre-determine sample sizes, due to the underlying system being deterministic. See Life Science Reporting Summary for additional details.

Parameter Value	SHOT-CA3I	SHOT-CA3E	REV	RO-CA1E	RO-CA1I
N	2000	2000	2000	2000 (1000, Figure 4F)	2000
t_{ref}	2 ms	2 ms	2 ms	2 ms	2 ms
t_m	10 ms	10 ms	10 ms	10 ms	10 ms
I^α	10 pA	-5 pA	-40 pA	-40 pA	-37.5 pA
v_{reset}	-65 mV	-65 mV	-65 mV	-65 mV	-65 mV
$v_{threshold}$	-40 mV	-40 mV	-40 mV	-40 mV	-40 mV
τ_d	20 ms	20 ms	20 ms	5 ms	20 ms
τ_r	2 ms	2 ms	2 ms	2 ms	2 ms
g (FORCE)	0.1	0.1	N/A	N/A	N/A
q (FORCE)	15	15	N/A	N/A	N/A
C_E (FORCE)	200	200	N/A	N/A	N/A
C_I (FORCE)	200	200	N/A	N/A	N/A
Δ_t (FORCE)	0.5 ms	0.5 ms	N/A	N/A	N/A
μ^{-1} (FORCE)	0.0025 ms	0.0025 ms	N/A	N/A	N/A
θ_{INT}	8.5 Hz	N/A	N/A	N/A	N/A
θ_{MS}	2-12 Hz	N/A	N/A	N/A	N/A
κ	1-1.5 (varies)	N/A	N/A	N/A	N/A
I^{GABA}	-10 pA	0 pA	0 pA	0 pA	0 pA
FORCE Training Time	19 s	19 s	N/A	N/A	N/A

Table 1: The parameters used for the SHOT-CA3 neurons, the reversion interneurons, and RO-CA1 excitatory and inhibitory populations. For all networks, we use an integration time step of $dt = 0.05$ ms and Euler integration. Some of the parameters are not applicable (N/A). Also note that the background current to neurons can also vary depending on the presence/absence of INP-MS. See Further Methods for Figures for more details.

Experimental Constraints Used to Build the Model	
Medial Septum (MS) inhibits interneurons via GABAergic connections to the hippocampus.	[45, 62, 63]
MS controls frequency of LFP, and population activities in hippocampus.	[40, 42, 64]
Overall activity in the MS drops during SPW-Rs.	[45]
Hippocampus can internally generate theta sequences.	[6, 7]
MS is critical for theta sequences.	[7]
Limited recurrent excitation in CA1.	[65]
Single trial learning, compression, reverse compression of spike sequences.	[5, 37]
Intrahippocampal Theta Oscillations	[14–16, 66–69].
Model Postdictions	
Phase precession of excitatory neurons.	[10]
Creation of internally generated theta sequences.	[6, 7]
Theta sequences can be compressed into SPWs.	[70, 71]
Gamma assembly formation nested on theta oscillation, and SPW-Rs.	[72, 73]
Sharp wave compression ratio is higher than theta phase precession compression ratio.	[3, 37, 45, 74]
Stochastic SPW initiation (via recurrent excitation) with unimodal inter-event-intervals.	[35]
Multi-modal inter-sharp-wave interval distributions.	[36]
Interneurons are phase-locked to ripple oscillations	[75–77]
Limitations of the Model	
Phase precession of interneurons (limited documentation [19],[43]).	
Internally generated theta sequences are not periodic.	[6]
Gamma from CA3 is significantly higher in the model than in data.	[59, 78–80]
Evidence of attractor/assembly dynamics in CA3.	[45]
Model Predictions	
Driving the MS continuously changes theta sequence order, phase precession slopes.	
Driving the MS changes replay structure from single to clustered SPW-Rs.	
Driving the MS changes peak gamma frequencies in the hippocampus.	
Interneuron sequences exist (some evidence, see [44]) and are critical for learning.	
Phase recession and sequence reversal possible when $\theta_{MS} > \theta_{INT}$.	
Extrinsic sequences in CA1 bound to interneuron sequences in CA3 indirectly via Schaffer Collaterals.	
A population of interneurons firing a synchronized burst with variable rates can reverse a replay.	
A combination of local and global inhibitory connections creates compressible sequences in the hippocampus.	
When MS is off, driving excitatory and inhibitory neurons in CA3 creates periodic SPWs (more regular distribution).	
Perturbation of the Entorhinal Cortex destroys learning.	
Blocking OLM cells during quiet awake disrupts reverse replay.	
Shutting down CA1 interneurons leads to assembly overlap.	

Table 2: Table summarizing the relationship between our network model, and the experimental literature.

Bibliography

[51] Hines, M. L., Morse, T., Migliore, M., Carnevale, N. T. & Shepherd, G. M. Modeldb: a database to support computational neuroscience. *Journal of computational neuroscience* **17**, 7–11 (2004).

[52] Sauvage, F. Learning in spiking neural networks. *Master Thesis, Imperial College London* (2016).

[53] Sussillo, D. & Abbott, L. F. Generating coherent patterns of activity from chaotic neural networks. *Neuron* **63**, 544–557 (2009).

[54] Harish, O. & Hansel, D. Asynchronous rate chaos in spiking neuronal circuits. *PLoS Comp. Bi* **11**, e1004266 (2015).

[55] O'keefe, J. & Burgess, N. Dual phase and rate coding in hippocampal place cells: theoretical significance and relationship to entorhinal grid cells. *Hippocampus* **15**, 853–866 (2005).

[56] Orchard, J., Yang, H. & Ji, X. Does the entorhinal cortex use the fourier transform? *Front. in Comp. Neuro.* **7**, 179 (2013).

[57] Heusser, A. C., Poeppel, D., Ezzyat, Y. & Davachi, L. Episodic sequence memory is supported by a theta–gamma phase code. *Nat. Neuro.* **19**, 1374 (2016).

[58] Lisman, J. & Buzsáki, G. A neural coding scheme formed by the combined function of gamma and theta oscillations. *Schiz. Bull.* **34**, 974–980 (2008).

[59] Lopes-dos Santos, V. *et al.* Parsing hippocampal theta oscillations by nested spectral components during spatial exploration and memory-guided behaviour. *Neuron* (2018).

[60] Nesse, W. H., Borisyuk, A. & Bressloff, P. C. Fluctuation-driven rhythmogenesis in an excitatory neuronal network with slow adaptation. *J. Comp. Neuro.* **25**, 317 (2008).

[61] Whittington, M. A., Traub, R., Kopell, N., Ermentrout, B. & Buhl, E. Inhibition-based rhythms: experimental and mathematical observations on network dynamics. *Int. J. of Psychophys.* **38**, 315–336 (2000).

[62] Freund, T. F. & Antal, M. Gaba-containing neurons in the septum control inhibitory interneurons in the hippocampus. *Nature* **336**, 170–173 (1988).

[63] Gulyás, A., Görcs, T. & Freund, T. Innervation of different peptide-containing neurons in the hippocampus by gabaergic septal afferents. *Neuroscience* **37**, 31–44 (1990).

[64] King, C., Recce, M. & O'keefe, J. The rhythmicity of cells of the medial septum/diagonal band of broca in the awake freely moving rat: relationships with behaviour and hippocampal theta. *Eur. Jour. of Neuro.* **10**, 464–477 (1998).]

[65] Deuchars, J. & Thomson, A. Ca1 pyramid-pyramid connections in rat hippocampus in vitro: dual intracellular recordings with biocytin filling. *Neuroscience* **74**, 1009–1018 (1996).

[66] Kramis, R., Vanderwolf, C. & Bland, B. H. Two types of hippocampal rhythmical slow activity in both the rabbit and the rat: relations to behaviour and effects of atropine, diethyl ether, urethane, and pentobarbital. *Exp. Neurol.* **49**, 58–85 (1975).

[67] Konopacki, J., Maciver, M. B., Bland, B. H. & Roth, S. H. Theta in hippocampal slices: relation to synaptic responses of dentate neurons. *Brain Res. Bull.* **18**, 25–27 (1987).

[68] Ferguson, K. A., Chatzikalymniou, A. P. & Skinner, F. K. Combining theory, model, and experiment to explain how intrinsic theta rhythms are generated in an in vitro whole hippocampus preparation without oscillatory inputs. *eNeuro* **4**, ENEURO–0131 (2017).

[69] Amilhon, B. *et al.* Parvalbumin interneurons of hippocampus tune population activity at theta frequency. *Neuron* **86**, 1277–1289 (2015).

[70] Lee, A. K. & Wilson, M. A. Memory of sequential experience in the hippocampus during slow wave sleep. *Neuron* **36**, 1183–1194 (2002).

[71] Nádasdy, Z., Hirase, H., Czurkó, A., Csicsvari, J. & Buzsáki, G. Replay and time compression of recurring spike sequences in the hippocampus. *J. Neuro.* **19**, 9497–9507 (1999).

[72] Csicsvari, J. *et al.* Massively parallel recording of unit and local field potentials with silicon-based electrodes. *J. Neurophys.* **90**, 1314–1323 (2003).

[73] Csicsvari, J., Jamieson, B., Wise, K. D. & Buzsaki, G. Mechanisms of gamma oscillations in the hippocampus of the behaving rat. *Neuron* **37**, 311–322 (2003).

[74] Skaggs, W. E., McNaughton, B. L., Wilson, M. A. & Barnes, C. A. Theta phase precession in hippocampal neuronal populations and the compression of temporal sequences. *Hippocampus* **6**, 149–172 (1996).

[75] Klausberger, T. *et al.* Brain-state-and cell-type-specific firing of hippocampal interneurons in vivo. *Nature* **421**, 844 (2003).

[76] Klausberger, T. *et al.* Spike timing of dendrite-targeting bistratified cells during hippocampal network oscillations in vivo. *Nat. Neuro.* **7**, 41 (2004).

[77] Klausberger, T. *et al.* Complementary roles of cholecystokinin-and parvalbumin-expressing gabaergic neurons in hippocampal network oscillations. *J. Neuro.* **25**, 9782–9793 (2005).

[78] Bieri, K. W., Bobbitt, K. N. & Colgin, L. L. Slow and fast gamma rhythms coordinate different spatial coding modes in hippocampal place cells. *Neuron* **82**, 670–681 (2014).

[79] Montgomery, S. M. & Buzsáki, G. Gamma oscillations dynamically couple hippocampal ca3 and ca1 regions during memory task performance. *Proc. of Nat. Acad. of Sci.* **104**, 14495–14500 (2007).

[80] Colgin, L. L. *et al.* Frequency of gamma oscillations routes flow of information in the hippocampus. *Nature* **462**, 353 (2009).